INFN - Laboratori Nazionali di Frascati
Servizio Documentazione

LNF-91/060 (IR)
2 Settembre 1991

OPTICAL DESIGN FOR GILDA, A BENDING MAGNET BEAMLINE AT THE E.S.R.F.

S. Pascarelli, F. Boscherini, A. Marcelli,
INFN, Laboratori Nazionali di Frascati, P.O. Box 13, I-00044 Frascati (Rome), Italy

S. Mobilio
Dipartimento di Energetica, Università dell'Aquila, Roio Monteluco, L'Aquila, Italy,
and INFN, Laboratori Nazionali di Frascati, P.O. Box 13, I-00044 Frascati (Rome), Italy

ABSTRACT

In this report we give a detailed description of the optics for GILDA, the Italian Collaborating Research Group beamline at the European Synchrotron Radiation Facility Ray–tracing simulations and simple calculations are used to discuss the effects which determine flux, resolution and spot size. Depending on the energy (in the range 5 to 50 keV) we expect fluxes between $3x10^{10}$ and $6x10^{12}$ photons/second, a resolution between $3x10^{-5}$ and $2x10^{-4}$ and spot sizes usually less than 1 mm.

1 - INTRODUCTION

The purpose of the present report is to describe the status of the project of the General purpose Italian beamLine for Diffraction and Absorption (GILDA), that will be installed on a bending magnet port of the European synchrotron radiation machine, ESRF. GILDA, proposed by a collaboration of several research groups belonging to different Universities, Consiglio Nazionale delle Ricerche (CNR) laboratories and to Laboratori Nazionali di Frascati (LNF), has been financed by the CNR and by the Istituto Nazionale di Fisica Nucleare (INFN). The main purpose of the beamline is to provide the Italian community working with synchrotron radiation in the x–ray region an easy access to the European Synchrotron Radiation Facility to perform experiments that require an intense and brilliant x–ray source, which is not available at the moment in Italy. GILDA will be fully equipped to routinely perform x–ray absorption, scattering and powder diffraction measurements. Moreover it will give the opportunity to install experimental apparata for other kinds of measurements.

The time schedule of GILDA foresees the design, construction and test of the beamline and of the experimental apparata during 1991 and 1992. In 1993 the beamline will be installed at ESRF to be ready to utilize the "first" x–ray photon planned in the autumn of 1993.

In the following we give a description of the performance of GILDA without considering certain "real world" aspects such as errors in clamping, vibrations and so on. In this sense the values listed here are to be considered as an optimal performance goal.

2 - GENERAL DESCRIPTION OF GILDA

The experiments to be performed on GILDA need an x–ray photon beam in the energy interval 5 - 50 KeV, with an energy resolution between 10^{-5} - 10^{-4}, a millimeter spot size, and a flux at the sample position up to 10^{11} -10^{12} photons/s. To achieve the above mentioned characteristics the beamline will work in different configurations. At low energy (5 - 22 KeV) the photon beam will be focussed both in the horizontal and vertical directions with the help of a monochromator and of two mirrors respectively; at high energy (22 - 50 KeV) no mirrors will be used, therefore the photon beam will be focussed only in the horizontal direction by the monochromator.

The general layout of the beamline is shown in Fig. 1. The photon beam from the storage ring travels at 1400 mm from the experimental floor. The front end between the storage ring and GILDA, all inside the machine hall, will be provided by ESRF. It will collect 6 mrad of horizontal divergence of radiation emitted from a bending magnet of 19.2 KeV of critical energy and will end at the shielding wall with a cooled 0.5 mm thick Be window, 20 m from the storage ring. The 36 m long beamline after the Be window will be completely constructed by the GILDA collaboration.

In the low energy configuration, configuration A (Fig. 2), a first mirror M_1, at ~ 25 m from the source, will intercept the radiation at a glancing angle of 3 mrad deflecting the beam in the vertical direction. At ~ 37.5 m from the source a double crystal fixed exit monochromator will be installed. It not only monochromatizes but also focusses the beam in the horizontal plane (sagittal focussing), as the second crystal will be curved. At ~ 40 m from the source a second mirror M_2 again deflects the photon beam in the vertical plane; in such a way after M_2 the beam propagates in the horizontal direction at a height of 140 mm above the storage ring level, a total of 1540 mm from the experimental floor.

In the high energy configuration, named hereafter configuration B (Fig. 3), mirrors M_1 and M_2 will be removed and the beam will not be focussed in the vertical plane. In such a configuration the vertical displacement of the beam is provided only by the monochromator and amounts to 50 mm. The beam is still focussed in the horizontal plane by the monochromator.

By changing the radius of curvature of mirror M_2 and of the second crystal the beam is focussed at 3 different focal points: E_1 at 50 m, E_2 at 54 m and E_3 at 58 m from the source. The three focal points E_1, E_2 and E_3 will be at the center of three different hutches, where the experimental apparata will be installed. Hutch 1 will be dedicated to scattering and diffraction experiments, hutch 2 to x–ray absorption experiments and hutch 3 to other experiments. In the original proposal a Reflexafs apparatus and a UHV chamber for surface studies have been financed for this last hutch.

3 - BEAMLINE AND OPTICS

3.1 - GENERAL CONSIDERATION

In the following we shall give a detailed description of the source, the monochromator and the two optical configurations. To evaluate the performance of the whole system we have carried out a double front analysis. First, pocket calculator type calculations yielded rough estimates, then a thorough ray–tracing analysis has been performed. In the simulations, values of 5, 20 and 50 KeV have been chosen to represent the three energy ranges (low, intermediate and high) respectively. The ray–tracing calculations enabled us to visualize actual intensity and power distributions on all optical elements and on the image planes, including aberrations, and to check the sensitivity to misalignment and shape variations of the optical elements. Furthermore, a more

accurate estimate of the total transmission of the beamline and of the energy resolution were obtained.

For the ray–tracing, we used the SHADOW [1] software package developed by F. Cerrina at the University of Wisconsin. It computes the propagation of a photon beam through an optical system. The program is designed to provide an optimal simulation of synchrotron radiation sources.

The parameters which determine the spectral range of the beamline are the grazing angle θ of the photon beam on the mirror surfaces and the metal coating of the mirrors themselves. For a given wavelength λ a critical grazing angle θ_c exists, given by:

$$\sin\theta_c \sim \theta_c = \sqrt{(N.r_0/\pi)}$$

where $N = \rho \cdot Z/A$ is the electron density for a material with atomic number Z, atomic weight A and density ρ and r_0 is the classical electron radius. At a fixed grazing angle, wavelengths shorter than the value given by the above relation are not reflected by the mirror. For x–rays, values for θ_c are of the order of some mrads or less. We have chosen the value of $\theta = 3$ mrad in order to have total reflection up to energies well above ~ 20 KeV.

Fig. 4 shows, as an example, the reflectivity of a Rh coated mirror at 3 mrad of grazing incidence. We observe that in this geometry M_1 will totally reflect x–rays with energies in the range 5 KeV to 22 KeV. The reflectivity decreases sharply at this energy for two combined effects: at a grazing angle of 3 mrad all energies above 22.5 KeV are absorbed and at 23.2 KeV Rh has its K absorption edge. We are also considering coatings with higher Z metals which would allow a higher upper limit for the energy, even if they present absorption edges in the energy range of utilization. At the moment no final decision on the mirror coating has been taken.The most important problem suffered by mirrors and crystals exposed to high intensity radiation is heat load, which can distort or damage the surface. For diffracting crystals, the heat load may cause great distortions of the diffracting planes, so that there is a large reduction in the transmitted flux from a two crystal system. In order to calculate the value of the power density consider the power emitted by the bending magnet, which is a function of the angle of elevation from the horizontal [2]:

$$P\ [\ W\ /\ \text{mrad}\phi \cdot \text{mrad}\psi] = 1285.6\ F(\gamma\psi)$$

where

$$F(\gamma\psi) = \{7/16 + 5/16\ (\gamma\psi)^2\ /\ [1 + (\gamma\psi)^2]\}\ [1 + (\gamma\psi)^2]^{-5/2}$$

where $\gamma = E/m_0c^2$, ϕ is the horizontal opening angle and ψ is the angle of elevation from the orbit plane. For an unlimited vertical acceptance:

$$P' = 73.0\ \text{Watts}\ /\ \text{mrad}\phi$$

A fan of 6 mrad of radiation is collected at the bending magnet port, therefore the total power entering the beamline is:

$$P = 438.0\ \text{Watts}$$

We have used the TRANSMIT code to compute the source spectrum as well as the power transmitted or reflected by the optical elements. Fig. 5 shows the variations in the power spectrum emitted by the bending magnet (curve a) as the photons are transmitted by a 500 μm Be window (curve b), and finally reflected by the first mirror M_1 (curve c).

Table I lists the values of the peak power densities on each element .

TABLE I - Power densities.

Location	Incident Power [W]	Absorbed Power [W]	Peak power density [W/mm^2]
From bending magnet	437.6		
Be window (20m)	437.6	52.3	1.4
Rh coated mirror (25m, 3mrad)	385.3	195.6	$2.3\ 10^{-3}$
First crystal, config.A	189.7		0.17
First crystal, config. B	385.3		0.35

3.2 - THE SOURCE

ESRF is a high energy, low emittance storage ring; its characteristics are reported in Table II [3].

TABLE II - Machine Characteristics.

electron beam energy	E = 6 GeV
current in multibunch mode	I > 100 mA
current in single bunch mode	I = 5 mA
radio frequency	RF = 352 MHz
circumference	C = 844 m
number of bunches	N = 1-992
horizontal emittance	$\varepsilon_x = 6.3 \cdot 10^{-9}$ m rad
vertical emittance	$\varepsilon_z \leq 6.3 \cdot 10^{-10}$ m rad
beam lifetime	τ > 12 h
magnetic field	0.8 T
critical energy of bending magnet	E_c = 19.2 KeV

Energetic electrons emit a highly collimated and intense flux of high energy photons, while a high brilliance is obtained due to a low emittance. The flux and brilliance of synchrotron radiation emitted from the bending magnet of ESRF are shown in Fig. 6 as functions of energy. Fig. 7 shows the brightness as a function of ψ at 5, 20 and 50 KeV: F_σ and F_π are the two polarization components of the radiation. In Fig. 8 we plot the linear and circular polarization coefficients as functions of ψ at the same energies.

The characteristics of the electron and photon bending magnet source are listed in Table III [3]:

TABLE III - Source electron and photon beam parameters.

electron beam				photon beam	
σ_x (μm)	σ_z(μm)	$\sigma_{x'}$ (μrad)	σ_z(μrad)	$\Delta\phi$(mrad)	σ_r (μrad) at critical energy
187	128	115	5	6	49

The electron beam in the bending magnet has a very low vertical divergence, ten times lower than the radiation's natural divergence at the critical energy, and about seven times smaller than the lowest value of σ_r (at 50 KeV). Therefore we shall neglect the convolution between the vertical divergence distributions of the emitted photons (σ_r) and the electron beam ($\sigma_{z'}$).

A 5000-ray simulation of the bending magnet source is shown in Fig. 9 (the units are cm.). The RANDOM/RANDOM source modelling type was used (i.e. rays in real and momentum space are randomly generated), with a gaussian space distribution and a synchrotron

source depth and angle distribution. In Fig. 10 we show vertical phase space z-ψ at the source point, considering a photon vertical divergence of $\pm 3\sigma_r$ at the critical energy.

3.3 - OPTICAL CONFIGURATION A

Fig. 2 shows the basic layout of the beamline in this configuration. Since both transmission and resolution are maximized by reducing the divergence of the beam on the monochromator, mirror M_1 transforms the diverging rays into a quasi parallel beam, and mirror M_2 focusses the monochromatic beam on the image planes E_1, E_2 and E_3. The demagnification is given by the ratio of the distance between the image point and mirror M_2 and the distance between the source and the mirror M_1. The focussing parameters are listed in Table IV.

TABLE IV - A Focussing parameters. p = distance from source to M_1; q = distance from image to M_2; m_v = q/p = vertical demagnification.

E_1			E_2			E_3		
p	q	m_v	p	q	m_v	p	q	m_v
(m)	(m)		(m)	(m)		(m)	(m)	
25	10	0.40	25	14	0.56	25	18	0.72

We will estimate the curvatures of the mirrors in the cylindrical approximation, where the ideally parabolic or elliptical surface needed is substituted by a cylinder of radius R_t. This is justified by the fact that the curvatures are typically of the order of kilometers, as we shall see. In this approximation, the relation between R_t, the source and image distances p and q and the grazing angle θ is :

$$(1)\quad 1/p + 1/q = 2/R_t.\sin\theta$$

In order to obtain a high resolution with a minimum loss of intensity it is necessary to reduce the vertical divergence of the rays impinging on the first crystal of the monochromator as much as possible; this is accomplished by adopting a collimating profile for M_1. A mirror in the form of a paraboloid of revolution with axis parallel to the $\psi = \phi = 0$ direction converts a photon beam coming from a point source situated in its focus into a parallel beam. The vertical divergence of the photon beam after the mirror, $\Delta\psi_0$, is due only to the source vertical dimensions σ_z. In the case of ESRF:

$$\Delta\psi_0 = 2.35 \cdot \sigma_z / p \sim 12\ \mu\text{rad} = 2.5\ \text{arc seconds}$$

This value of the intrinsic divergence implies that any spurious slope errors on the mirrors (e.g. manufacturing errors and heat load distorsions) should ideally be not greater than a few (1-2) arcsec. Fig. 11a shows z-ψ phase space of the photons at 30 m from the source after an ideal parabolic mirror (compare with Figure 10). As already pointed out, the ideal parabolical profile can be substituted by a circular profile of radius R_t due to the large value of R_t. In the cylindrical approximation an estimate of the radius of curvature of M_1 is obtained by setting $q = \infty$ in equation (1) :

$$R_t\,(\text{m}) = p\cdot(\,2 / \sin\theta\,) \sim 16.6\ \text{Km}$$

Ray-tracing simulations confirm that the aberrations introduced in this approximation are negligible as we see from Fig. 11b which shows z-ψ phase space of the photons at 30 m from the source after mirror M_1: the performance of the cylindrical mirror is as efficient as that of the

ideal parabolic mirror in this case. Table V reports some geometrical parameters of mirror M_1 (tentative).

TABLE V - Mirror M_1.

grazing angle θ(mrad)	length L (mm)	width H (mm)	radius R_t (km)	vertical acceptance $\Delta\psi$ (μrad)	exit vertical divergence $\Delta\psi_0$ (μrad)
3	1500	200	16.6	180	12

The second mirror, M_2, at 40 m from the source point, vertically focusses the quasi parallel monochromatic beam on the three sample positions.

The curvatures R_i (i = 1,2,3 refers to the three image planes F_i) for M_2 are obtained from equation (1) with $p = \infty$ and $q = q_i$ (see Table IV). Table VI contains information on the geometrical parameters of M_2.

TABLE VI - Mirror M_2.

granzing angle θ (mrad)	length L (mm)	width H (mm)	E_1 R_t (km)	E_2 R_2 (Km)	E_3 R_3 (Km)
3	1500	200	6.6	9.3	12.0

The vertical demagnification and spherical aberrations, δ_v , of the mirrors contribute to the vertical dimension in the image points E_1, E_2 and E_3. The smallest spot size is obtained for an optimum value of m_v M_{opt}, for which the sum of the two contributions is minimized [4] which depends on the vertical divergence of the beam on the mirror, on source size and distance of the source from the mirror. In our case $0.5 \leq M_{opt} \leq 0.6$, which is in good agreement with the values of m_v on the three hutches (see table IV). The value of δ_v can be estimated using the following relation [4]:

$$\delta_v \simeq 0.375 \cdot L^2/R \cdot | m_v - 1 |$$

where L is the length of the mirror intercepted by the rays. We will take L to be the FWHM of the beam profile on the mirrors. A third contribution comes from the sagittal focussing aberration induced by the monochromator, and will be discussed later.

Spherical aberrations could be avoided on hutch 1 and reduced on the other two by allowing mirror M_1 to do the vertical focussing instead of mirror M_2, which would be plane: in this case p = q (m_v, = 1) for hutch no.1. Not only, but higher magnifications would also lead to a better collimation of the beam on the focal spots, a must for diffraction measurements. This possibility has been studied in detail, and the results are summarized in Appendix A.

Since the source has a gaussian profile we expect the source size contribution to spot size to give a gaussian spot profile. As for the spherical aberration contribution, the spot profile is expected to be a convolution between the (gaussian) profile of the beam on the mirror and the rectangular window function due to the finite extent of the mirror; depending on the relative dimensions of the mirror and of the beam profile on the mirror (i.e. on the beam divergence) the result can be a quasi-rectangular distribution or a more gaussian profile, or intermediate.

3.4 - OPTICAL CONFIGURATION B

The basic layout of the beamline in this configuration is very simple (Fig. 3). There are only two optical elements: a slit S at 37.0 m and the monochromator at 37.5 m.

The vertical divergence of the beam impinging on the first crystal of the monochromator, $\Delta\psi$, is determined by the slit S. The divergence accepted by a slit of halfwidth s, at a distance D from the source, with $s \ll \sigma_r \cdot D$, is:

$$\Delta\psi\,(s) = (\,2 \cdot s + 2.35 \cdot \sigma_z\,) / D = \Delta\psi_1 + \Delta\psi_2$$

In this configuration the beam is not focussed in the vertical plane. The vertical spot size is determined by the slit width and the sagittal focussing aberration. The slit width contribution at a distance F from the source point is a rectangular distribution of width:

$$\Delta z_i = \Delta\psi_1 \cdot F + \Delta\psi_2 \cdot (F - D)$$

3.5 - THE MONOCHROMATOR

The monochromator is formed by two perfect Si crystals in the (+n,-n) configuration, diffracting in the plane perpendicular to the electron orbit. A schematic drawing of it is shown in Fig. 12. The first crystal is flat, while the second one is bent so as to assume a cylindrical shape with axis parallel to the beam direction. This geometry will focus the beam out of the plane of scattering (sagittal focussing), i.e. in the horizontal plane in the present case. The following relation holds for sagittal focussing:

$$(2)\quad 1/p + 1/q = 2\cdot\sin\theta/R_s$$

where R_s is the radius of curvature, θ the Bragg angle, and p and q are the source and image distances respectively. To keep the beam focus fixed at a constant distance from the curved crystal as the photon energy varies, the curvature R_s will be varied. Table VII shows values of R_s at 5 and 20 KeV for a Si (311) cut and at 50 KeV for a Si (511) cut at the three focal points.

TABLE VII - Values of the radius of curvature for sagittal focussing.

energy (KeV)	Bragg plane (hkl)	θ_B (degrees)	E_1 R_s(m)	E_2 R_s(m)	E_3 R_s(m)
5	311	49.2	14.2	17.4	20.1
20	311	10.9	3.6	4.3	5.0
50	511	6.8	2.2	2.7	3.2

The ideal geometry for a point-to-point focusing x–ray monochromator is one in which the reflecting planes are curved to confocal ellipsoids of revolution and the surface ground to the Rowland circle. In the monochromator this ideal crystal shape is approximated to a cylinder. Therefore, due to the horizontal divergence ϕ of the beam, only the rays impinging on the axis of the cylinder ($\phi = 0$) have the correct Bragg angle defined by the first crystal. Those being diffracted off axis ($\phi \neq 0$) will have an angle θ which differs from the Bragg condition by a quantity $\Delta\theta = \theta - \theta_B$, which is a function of ϕ. As long as $\Delta\theta$ remains smaller than the total width of the reflection curve (Darwin width or rocking curve width) the rays will be diffracted by the double crystal system, otherwise they will not be diffracted and there will be a loss in intensity [5].

For small Bragg angles the values of θ are found to be independent of the horizontal divergence ϕ only when the demagnification m_h is close to 1/3 [5]: in this geometry there is no loss of intensity associated with the mismatch in the Bragg angles between the first and the second crystal. We have chosen to satisfy this condition on the first of the three hutches E_1, at 50 m from the source point. Therefore the monochromator has been set at 37.5 m. It is

interesting to note that, in relation to the loss of intensity caused by the curved crystal, the higher the energy, the lower the useful horizontal acceptance $\Delta\phi$.

3.5.1 - ENERGY RESOLUTION

The energy resolution $\Delta E/E$ for a double crystal monochromator in the (+n,-n) configuration is given by the following equation:

$$(3)\quad \Delta E/E = \Delta\lambda/\lambda = \sqrt{(\omega^2 + \Delta\psi^2)} \cdot \text{cotg}\,\theta_B$$

where ω is the width of the total reflection curve for a perfect crystal (rocking curve) and $\Delta\psi$ is the total vertical divergence incident on the crystal, including natural divergence, source size effects and mirror imperfections. ω is a function of energy, Bragg angle and degree of polarization of the radiation. If the photons are linearly polarized with the electric vector in the plane perpendicular to the diffraction plane:

$$\omega = \omega_\sigma \sim \lambda^2 / \sin 2\theta_B$$

If the radiation is linearly polarized in the diffraction plane:

$$\omega = \omega_\pi = \omega_\sigma \cdot \cos 2\theta_B$$

Obviously, ω_π is smaller than ω_σ and $\Rightarrow 0$ for $\theta_B \Rightarrow 45°$.
In the limit $\Delta\psi \Rightarrow 0$, the resolution reaches its intrinsic value:

$$\Delta\lambda/\lambda^{(i)} = \omega \cdot \text{cotg}\,\theta_B$$

The intrinsic resolution is practically independent of energy, its value being (almost) uniquely determined by the choice of the diffraction planes. The smaller the Bragg plane spacing, d, the better the intrinsic resolution:

$$\Delta\lambda/\lambda^{(i)} \sim d^2$$

If a high energy resolution is required it is necessary to operate with high index diffraction planes. We have chosen, in the simulations, to use Si (311) for optical configuration A and Si (511) for optical configuration B. Table VIII lists values of $\Delta\lambda/\lambda^{(i)}$ for typical Si diffraction planes.

TABLE VIII - Intrinsic resolutions of some Si diffracting planes.

Bragg planes	d (Å)	$\Delta\lambda/\lambda^{(i)}$
Si (111)	3.135	$1.46 \cdot 10^{-4}$
Si (220)	2.715	$6.23 \cdot 10^{-5}$
Si (311)	1.637	$2.99 \cdot 10^{-5}$
Si (511)	0.957	$8.80 \cdot 10^{-6}$

The choice of the crystals therefore determines the beamline's resolution limit, which can be reached only if $\Delta\psi \Rightarrow 0$ (see eq. 3).

3.5.2 - TRANSMISSION

A rough estimate of the transmission of a double flat crystal monochromator in the (+n,-n) configuration can be obtained by a simple λ–ψ Du Mond space analysis. In fact, if $A = \Delta\psi \cdot \Delta\lambda$ is the total phase space area of the photons arriving on the first crystal in the interval $\Delta\lambda$, and $\alpha = \Delta\psi \cdot \lambda \cdot \omega \cdot \mathrm{cotg}\theta_B$ is the area of the transmitted strip (Fig. 13):

$$(4)\ T = \alpha/A = \lambda \cdot \omega \cdot \mathrm{cotg}\theta_B / \Delta\lambda = \omega / (\omega + \Delta\psi)$$

This calculation totally neglects the z–ψ phase space distribution of synchrotron radiation.

A more precise estimate of T is obtained by doing a z–ψ–λ phase space analysis. In any case, polarization effects, which are important with synchrotron radiation since the degree of polarization (and therefore the value of ω) is a function of energy and of vertical divergence ψ, as well as crystal reflectivities, still need to be taken into account.

Moreover, as we have already mentioned, bending the second crystal will cause the loss of photons with large horizontal divergence if ω is small.

If a high intensity is desired on the sample it is best to operate with crystals which have wide rocking curves. However, high transmissions can be obtained for any value of ω, provided $\Delta\psi \ll \omega$ (see eq. 4). In fact, if $\Delta\psi \Rightarrow 0$, $T \Rightarrow 1$.

3.5.3 - HORIZONTAL DEMAGNIFICATION

It is only the monochromator that determines the horizontal dimensions of the image. In the absence of sagittal focussing aberrations, the horizontal dimension Δx_i of the beam in the focal spot is:

$$\Delta x_i = m_h \cdot \Delta x_s$$

where Δx_s is the horizontal dimension of the source and m_h is the horizontal demagnification.

This contribution to the spot size will have a gaussian profile. We report the values of m_h in the three focal spots in Table IX.

TABLE IX - Horizontal demagnification.

	E_1	E_2	E_3
m_h	0.33	0.44	0.55

3.5.4 - HARMONIC REJECTION

A set of Bragg planes will provide an output beam that contains unwanted harmonic energies since higher orders of diffraction are unavoidable, if the structure factor does not vanish. Three factors determine the total harmonic content of the "monochromatized" beam on the sample:

1) the number of harmonic orders n = 2, 3, etc, allowed by the set of Bragg planes
2) the ratio of the number of photons of energy n·E and of energy E (the fundamental): $I^{(n)}/I^{(1)}$
3) the ratio of crystal reflectivity for the n^{th} harmonic and the fundamental: $R^{(n)}/R^{(1)}$.

If harmonic rejection is desired, Bragg planes with odd indexes should be used because the structure factor for the second harmonic vanishes for Si crystals [7]. In Table X we list values of $R^{(n)}/R^{(1)}$ and of $I^{(n)}/I^{(1)}$. $H^{(n)}$ is the intensity of the n^{th} harmonic on the sample.

TABLE X - Harmonic rejection.

energy (KeV)	Bragg planes (hkl)	n	$R^{(n)}/R^{(1)*}$	$I^{(n)}/I^{(1)}$	$H^{(n)}$
5	111	1	1.00	1.00	1.00
15		3	0.067	0.82	6.10^{-2}
20		4	0.038	0.69	3.10^{-2}
25		5	0.012	0.58	7.10^{-3}
5	220	1	1.00	1.00	1.00
10		2	0.163	0.93	2.10^{-1}
15		3	0.041	0.82	3.10^{-2}
20		4	0.012	0.69	8.10^{-3}
5	311	1	1.00	1.00	1.00
15		3	0.031	0.82	3.10^{-2}
20		4	0.013	0.69	1.10^{-2}
20	311	1	1.00	1.00	1.00
60		3	0.031	0.18	6.10^{-3}
80		4	0.013	0.07	1.10^{-3}
50	511	1	1.00	1.00	1.00
150		3	0.012	0.009	1.10^{-4}

* calculated for σ polarized radiation at $\lambda = 1.6$ Å [7].

Since we have chosen to use only Bragg planes with odd indexes, Si (311) and Si (511), the harmonic content is negligible. Anyhow the monochromator will allow the rejection of harmonics by a mismatch of the Bragg angle between the two crystals within the Darwin width.

3.5.5 - SAGITTAL FOCUSSING ABERRATION

The sagittal focussing geometry will introduce aberrations in the horizontal and vertical planes. For small Bragg angles, demagnifications, and horizontal acceptances, the total spatial dimensions due to aberrations on both the horizontal and vertical planes, $\Delta x^{(ab)}$ and $\Delta z^{(ab)}$, can be estimated as [6]:

$$\Delta x^{(ab)} \simeq p\,(\Delta\phi/2)^3\,(1+m_h)^2/(4\,m_h^2\,\theta^2)$$

$$\Delta z^{(ab)} \simeq p\,(\Delta\phi/2)^2\,(1+m_h)/(2\theta)$$

Therefore, the larger $\Delta\phi$ the stronger the aberrations. In Fig. 14a and 14b we report a simulated vertical phase space (at 20 KeV, with the monochromator focussing on the first hutch) after the monochromator at $\Delta\phi = 1$ mrad and $\Delta\phi = 6$ mrad to show this effect on the vertical divergence of the beam.

4 - PERFORMANCE OF THE OPTICAL SYSTEM

We have considered now all the contributions to resolution, transmission, horizontal and vertical spot size. Here we will compare them with ray–tracing simulation results which therefore include the effects of aberrations. Roughness and slope errors of mirrors and crystal surfaces have not been included.

The simulations are the result of nine independent 5000-ray source-generation / ray-tracing processes, summing up to a total statistics of 45000 randomly generated rays for the values reported in Tables XI - XVII and Figs. 15-16 and 19-21. All plots shown are instead generated from a single 5000-ray run.

4.1 - CONFIGURATION A

4.1.1 - ENERGY RESOLUTION

Ideally, in this configuration the energy resolution is determined only by the crystal intrinsic resolution and by the divergence of the beam after the first mirror due to the finite size of the source. In Fig. 15 we compare the values of the calculated energy resolution (neglecting aberrations) as a function of energy for several crystal cuts as well as the ray-tracing results for Si (311) for E = 5 and 20 KeV, reported as squares.

4.1.2 - TRANSMISSION

The total transmission is determined by the first mirror through its reflectivity and length, by the monochromator through the transmission of the first and second crystal and by the reflectivity and length of the second mirror. Fig. 16 shows the calculated flux on the first hutch and with a 6 mrad horizontal acceptance for several crystal cuts. In Table XI we list the results of the ray–tracing simulations. Absorption effects due to the beryllium windows on the beamline are not included. The values corresponding to the first hutch and to $\Delta\phi$=6 are also reported as squares on Fig. 16 for comparison. Notice that the horizontal acceptance of the monochromator is 6 mrads only for the first hutch. To obtain the values of flux for the other hutches one has to scale the values reported in Fig. 16 for the horizontal acceptance of the monochromator relative to the hutch considered. This quantity can be obtained, to a good approximation, from the ratio of the transmission of the monochromator at $\Delta\phi$=1 to that at $\Delta\phi$=6 mrad. The transmission is defined as the ratio between the number of rays per eV at the image and the number of rays per eV at the source.

TABLE XI - Total transmission in configuration A. R: reflectivity of the Rh coated mirrors M_1 and M_2 (θ = 3 mrad); GT_1: geometrical transmission of M_1 (θ = 3 mrad); GT_2: geometrical transmission of M_2 (θ = 3 mrad); T_M: transmission of the monochromator (Si 311); T: total beamline transmission; A: horizontal acceptance of the monochromator (mrads).

E (KeV)	hutch	R GT_1	T_M $\Delta\phi$=1 $\Delta\phi$=6	GT_2 $\Delta\phi$=1 $\Delta\phi$=6	T $\Delta\phi$=1 $\Delta\phi$=6	A
5	E_1,E_3	0.92 0.65	0.54	0.98	0.30	6
20	E_1	0.93 0.95	0.37. 0.37	0.99 0.81	0.30 0.24	6
	E_3	0.93 0.95	0.37 0.18	0.99 0.86	0.30 0.13	2.9

4.1.3 - FOCAL DIMENSION

Tables XII and XIII report the expected horizontal and vertical dimensions of the beam in E_1 and E_3 as evaluated by SHADOW and as expected on the basis of source size, sagittal and spherical aberrations (see section 3). Notice that for the sagittal aberrations calculation we have used the maximum horizontal acceptance of the crystal, not always equal to 6 mrad.
When comparing SHADOW results and the calculation (here and below) we must note that some contributions give a gaussian profile (source size) while others give a rectangular profile (usually spherical and sagittal aberration). The resulting profile is a convolution of these contributions which is hard to calculate analitically. Therefore in these comparisons we stress trends and try to identify which effects give dominant contributions while rigorous quantitative comparisons are sometimes difficult. The values listed as ray–tracing results are reasonable estimates of the dimensions. In some cases the blurring at the edges of the intensity profiles is quite large and should be taken into account when comparing ray–tracing results with calculations. Reference should be made to the plots of the spot size reported in figures 17 and 18 in these cases.

TABLE XII - Total horizontal spot size in configuration A (in microns).SHA: ray–tracing results; D: source size demagnification; SA.A.: sagittal aberration.

E	E_1			E_3		
(KeV)	SHA.	D	SA.A.	SHA.	D.	SA.A.
5	250	220	0	360	360	0
20	250	220	0	350	360	0

The value obtained with SHADOW are close to those expected from the source size; the sagittal aberration always gives a negligible contribution.

TABLE XIII - Total vertical spot size in configuration A (in microns). SHA: ray–tracing results ; D: source size demagnification; SP.A.: spherical aberration; SA.A.: sagittal aberration .

E	$\Delta\phi$	E_1				E_3			
(KeV)	(mrad)	SHA.	D.	SP.A	SA.A.	SHA	D.	SP.A.	SAA.
5	1	300	200	75	10	410	370	20	10
	6	500	200	75	260	410	370	20	300
20	1	305	200	25	30	440	370	5	40
	6	1330	200	25	1180	600	370	5	320

All three contributions to vertical image size are important and there is fair agreement between ray–tracing and calculation. Notice that at 20 keV for 6 mrad acceptance the sagittal aberrations become very large.

In Fig. 17 we show 5000-ray image simulations at 5 KeV in E_1 and E_3 for $\Delta\phi$ = 1 and 6 mrad. In Fig. 18 we show the same at 20 KeV.

4.2 - CONFIGURATION B

4.2.1 - ENERGY RESOLUTION

In this configuration the resolution is determined by the crystal intrinsic resolution and by the slit width, which determines the divergence at the monochromator. Fig. 19 reports the calculated resolution values for several crystal cuts and the ray-tracing results for Si (511).

4.2.2 - TRANSMISSION

The total transmission is determined by the slit and by the monochromator through the transmission of the first and second crystal (the losses are determined also by the horizontal acceptance). Fig. 20 reports the total flux in E_1 for several crystal cuts and with a 6 mrad horizontal acceptance. We list in Table XIV the results of the ray–tracing simulations, which are also reported on Fig. 20. Absorption effects due to the beryllium windows on the beamline are not included.

TABLE XIV - Total transmission in configuration B. GT_S: geometrical transmission of slit S; T_M: transmission of the monochromator (Si 511); T: total beamline transmission; A: horizontal acceptance of the monochromator (mrads).

E	GT_S	hutch	T_M	T	A
(KeV)			$\Delta\phi$=1 $\Delta\phi$=6	$\Delta\phi$=1=$\Delta\phi$=6	
50		E_1	0.13 0.11	0.02 0.02	5.1
slit=0.5 mm	0.15				
		E_3	0.08 0.02	0.01 0.003	1.5
50		E_1	0.06 0.05	0.02 0.02	5.0
slit=1.0 mm	0.31				
		E_3	0.05 0.01	0.02 0.003	1.2

4.2.3 - FOCAL DIMENSION

We report in the tables XV and XVI the horizontal and vertical spot sizes as evaluated by SHADOW and the magnitude of the various contributions described in section 3.

TABLE XV - Total horizontal spot size in configuration B (in microns). SHA: ray–tracing results ; D: source size demagnification; SA.A.: sagittal aberration.

slit	$\Delta\phi$	E_1			E_3		
(mm)	(mrad)	SHA.	D.	SA.A.	SHA.	D.	SA.A.
0.5	1	255	220	0	350	360	0
	6	355	220	220	350	360	0
1.0	1	255	220	0	350	360	0
	6	455	200	200	350	360	0

In this case there is a fair comparison between SHADOW and the calculations. Sagittal aberrations contribute considerably to source size in E_1.

TABLE XVI - Total vertical spot size in configuration B (in microns). SHA: ray-tracing results; S: Slit projection; SA.A.: sagittal aberration.

slit	$\Delta\phi$	E_1			E3		
(mm)	(mrad)	SHA.	S.	SA.A.	SHA.	S.	SA.A.
0.5	1	770	750	50	810	910	60
	6	2270	750	1400	1000	910	80
1.0	1	1270	1430	50	1770	1710	60
	6	2770	1430	1450	1770	1710	85

As predicted at this energy due to the small Bragg angles involved the sagittal aberrations causes a large deterioration of vertical dimension.

Fig. 21 and Fig. 22 show 5000-ray simulations for $\Delta\phi$ = 1 mrad and a 1.0 mm slit in E_1 and E_3 respectively.

ACKNOWLEDGEMENT

We wish to thank Manuel Sánchez del Rio for discussions and support during this study.

APPENDIX A

The possibility of occasionally using mirror M_1 as focussing mirror instead of mirror M_2, eliminating spherical aberrations on the first hutch as well as having an overall increase in beam collimation, has been considered in detail and finally rejected. The reasons for this lie mainly in the fact that, in comparison to the "M_1 = collimating mirror" geometry, the increase in beam collimation in the "M_1 = focussing mirror" geometry is not strong enough to compensate for the decrease in both transmission and resolution, due to the fact that the beam impinging on the first crystal diverges.

Ray–tracing simulations have been performed for both geometries using Si (311) crystals and the results show that, once beam divergence is fixed by the use of slits, energy resolution and beamline transmission are considerably better in the "M_1 = collimating mirror" geometry. As for the spherical aberrations, the spot sizes in the "M_1 = collimating mirror" geometry are smaller, as one would expect on the basis of a comparison between demagnification (magnification) m_v with values for M_{opt}: m_v = 0.40, 0.56, 0.72 with $0.5 \leq M_{opt} \leq 0.6$ and m_v = 1.00, 1.16, 1.32 with $M_{opt} \leq 0.4$. Table XVII summarizes some of the results obtained in this analysis.

TABLE XVII

E (KeV)	geometry	$\Delta\phi$ (mrad)	$\Delta E/E$	T	$\Delta x \cdot \Delta z$ (mm)	$\Delta z'$ (μrad)
		1		0.07	0.25· 0.30	50
5	coll		$3 \cdot 10^{-5}$			
		6		0.04	0.25 · 0.40	50
		1			0.25 · 0.55	50
5	foc		$5 \cdot 10^{-5}$	0.04		
		6			0.25 · 0.61	50
		1	$5 \cdot 10^{-5}$	0.10	0.25 · 0.30	50
20	coll					
		6	$7 \cdot 10^{-5}$	0.07	0.25 · 1.20	100
		1		0.04	0.25 · 0.50	50
20	foc		$2 \cdot 10^{-4}$			
		6		0.03	0.30 · 1.22	100

REFERENCES

[1] B. Lai and F. Cerrina, "SHADOW: A Synchrotron Radiation Ray–tracing Program"; Nucl. Instr. and Meth. A246, 337 (1986).

[2] G. K. Green, "Spectra and Optics of Synchrotron Radiation" (1976); Brookhaven National Laboratory, Upton, New York.

[3] ESRF Red Book

[4] G. Förstner, M. Krisch, and J. Susini, SRI '91 Proceedings.

[5] C.J. Sparks, Jr., B.S. Borie, and J.B. Hastings, Nucl. Instr. and Meth. 172 (1980) 237-242.

[6] G.E. Ice and C.J. Sparks, Jr., Nucl. Instr. and Meth. 222 (1984) 121-127.

[7] R. Caciuffo, S. Melone, F. Rustichelli, and A. Boeuf, Physics Reports 152 (1987) 1-71.

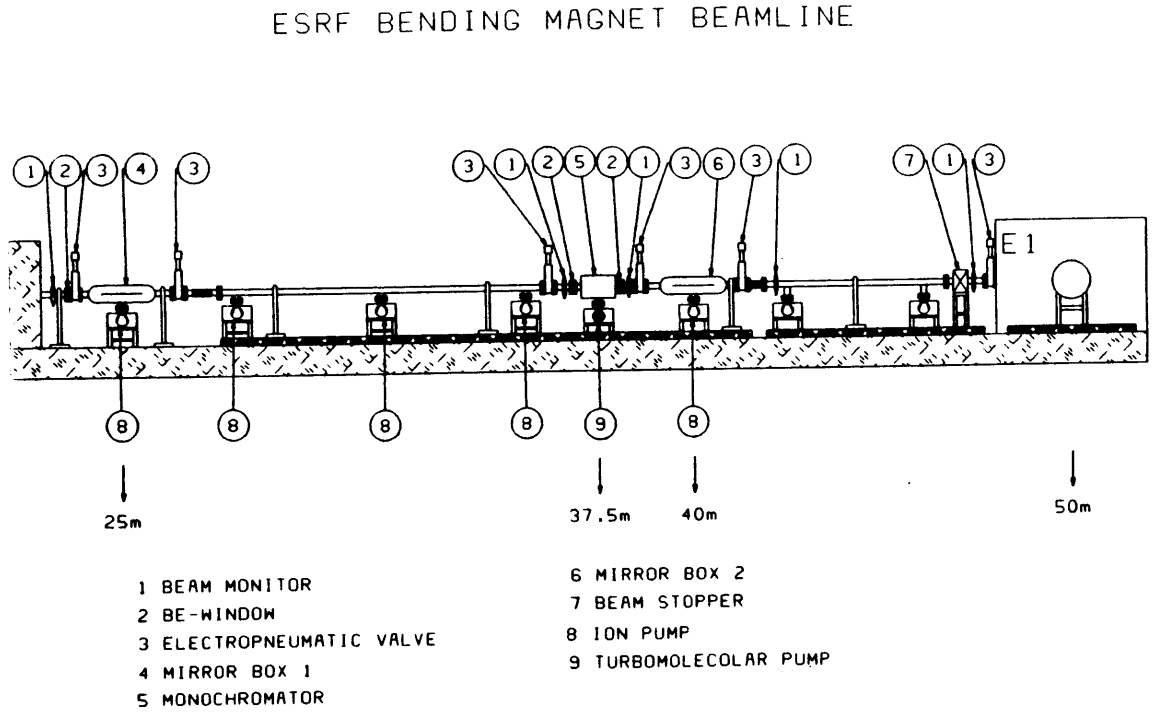

FIG. 1 - General layout of the beamline. The main components are two mirrors, the monochromator and three experimental stations. Not all details are definitive at this time.

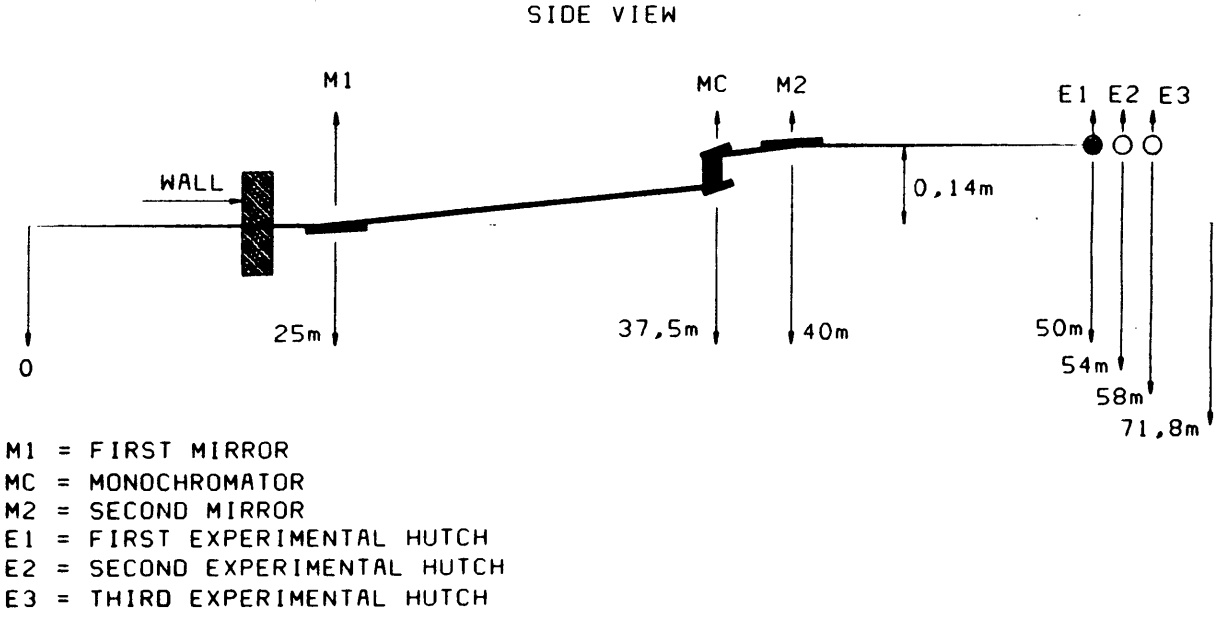

FIG. 2 - Schematic representation of beam path for configuration A (for low energy).

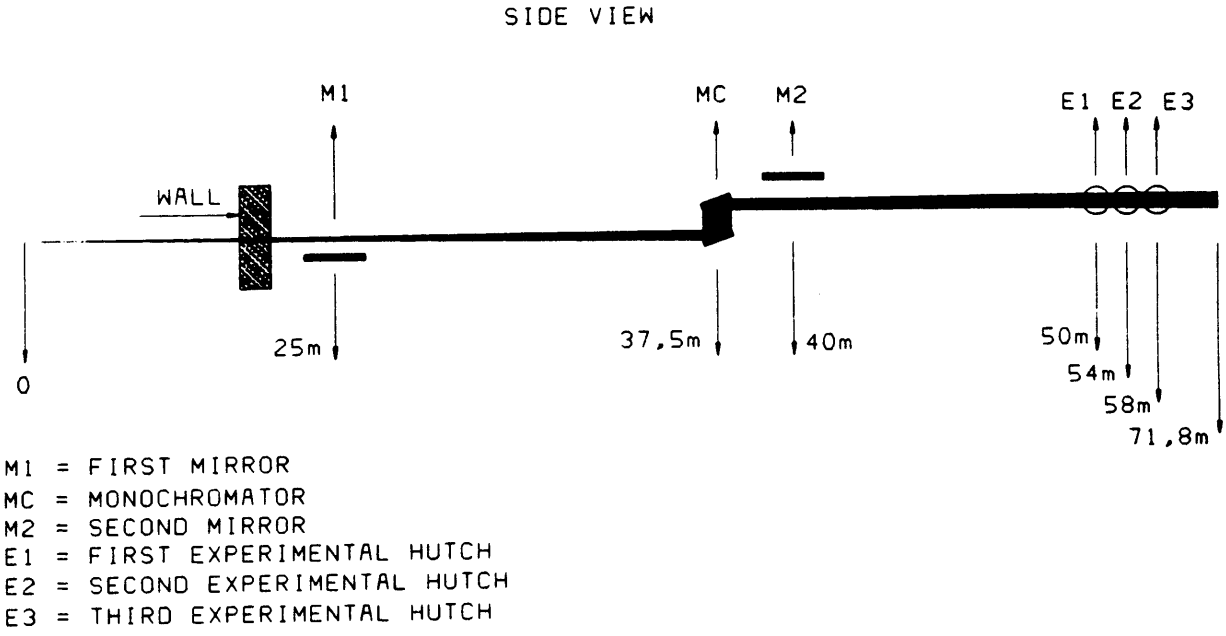

FIG. 3 - Schematic representation of beam path for configuration B (for high energy).

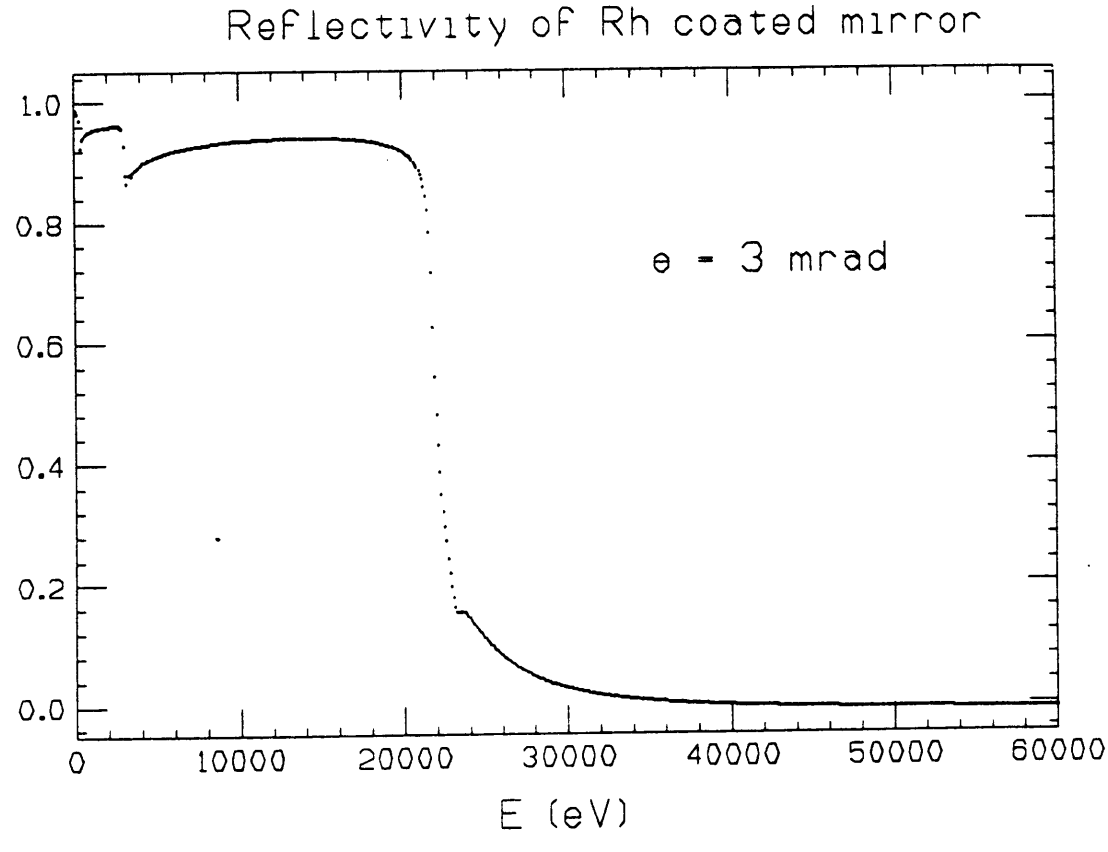

FIG. 4 - Reflectivity of a Rh coated mirror at a grazing angle of 3 mrads.

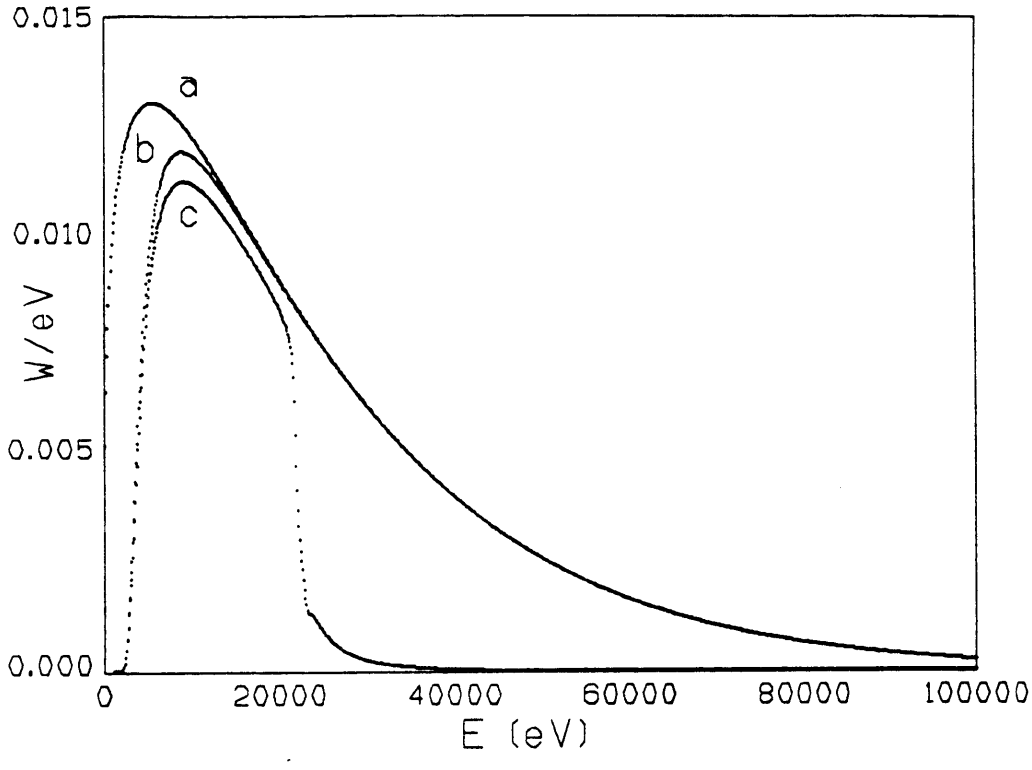

FIG. 5 - Power density as a function of energy (a) as emitted from the source, (b) after 0.5 mm Be, and (c) after the Rh coated mirror.

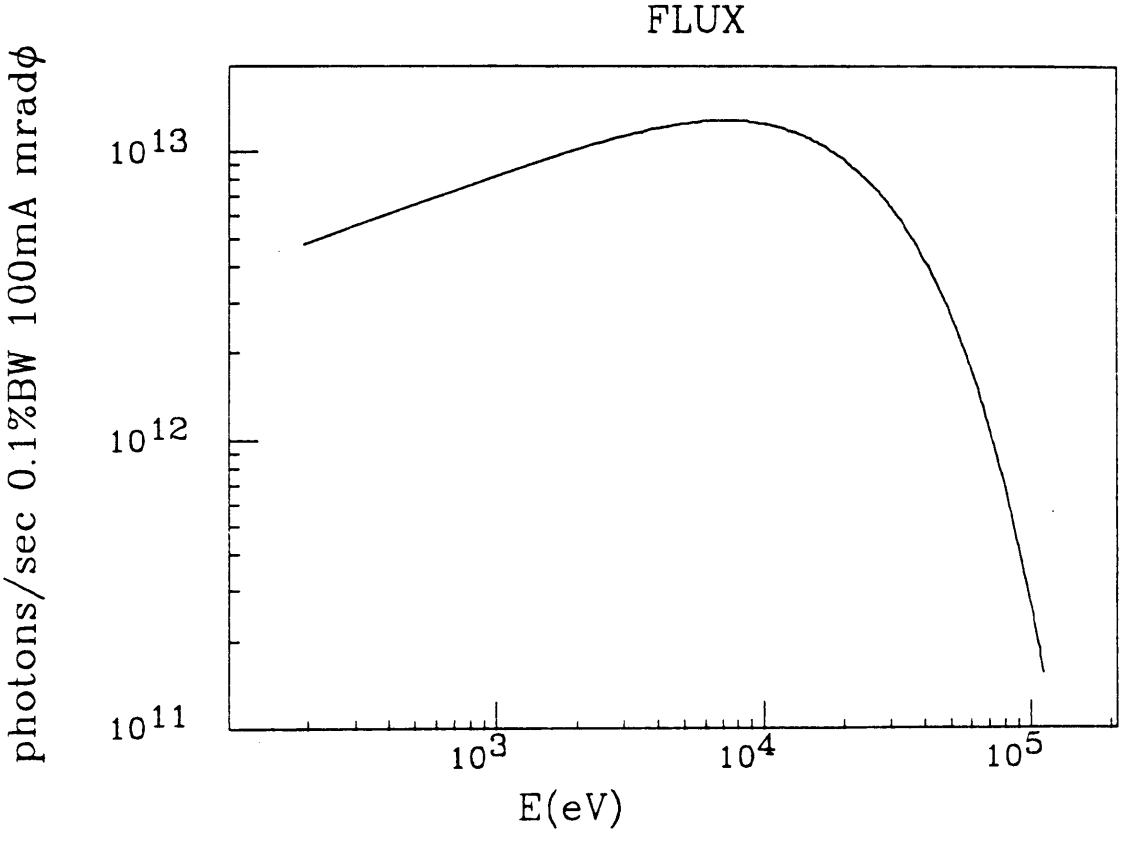

FIG. 6a - Flux emitted from the ESRF bending magnet source.

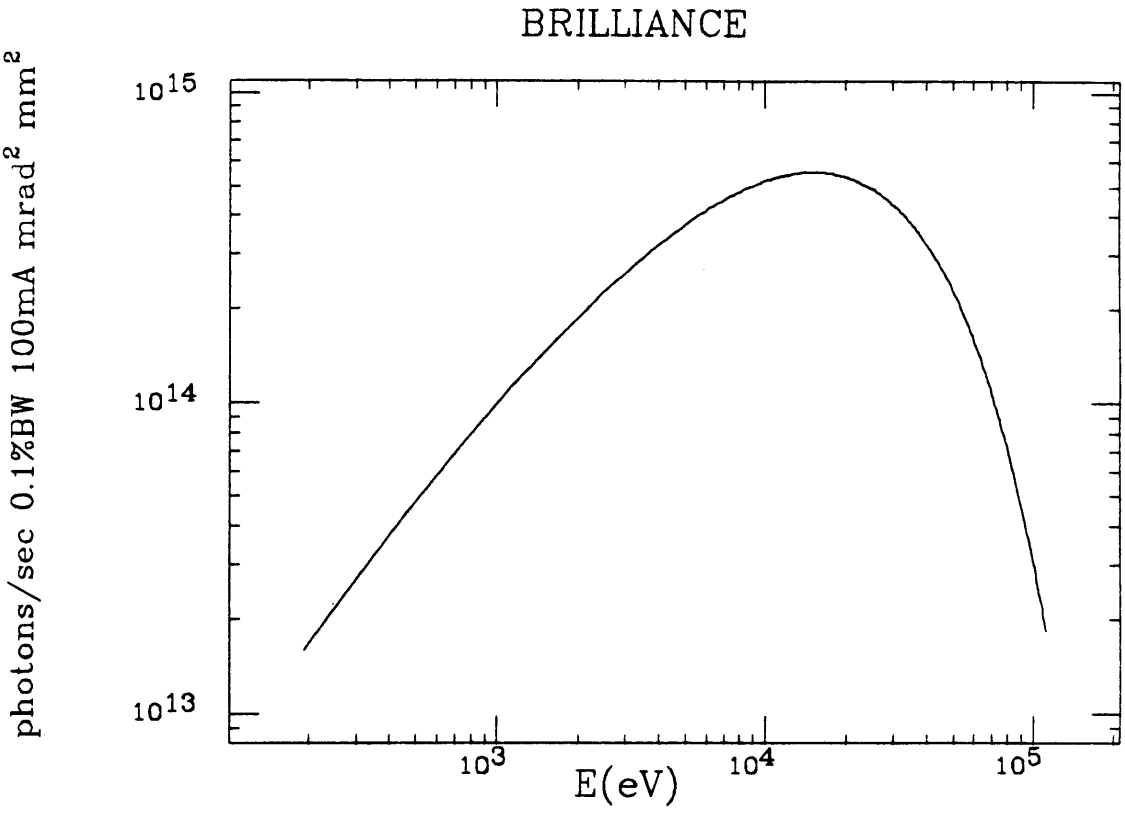

FIG. 6b - Brilliance emitted from the ESRF bending magnet source.

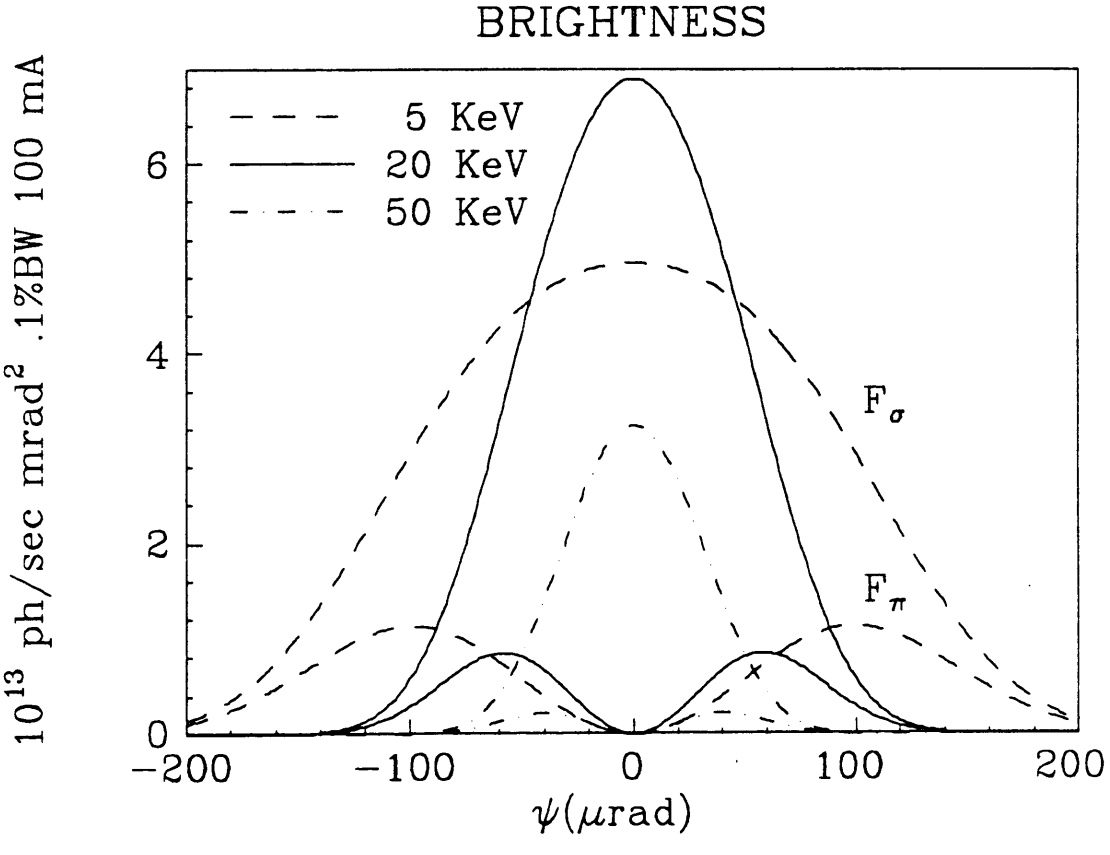

FIG. 7 - Brightness emitted from the ESRF bending magnet source for π and σ components at 5, 20, and 50 keV, as a function of angle of elevation from the orbit plane.

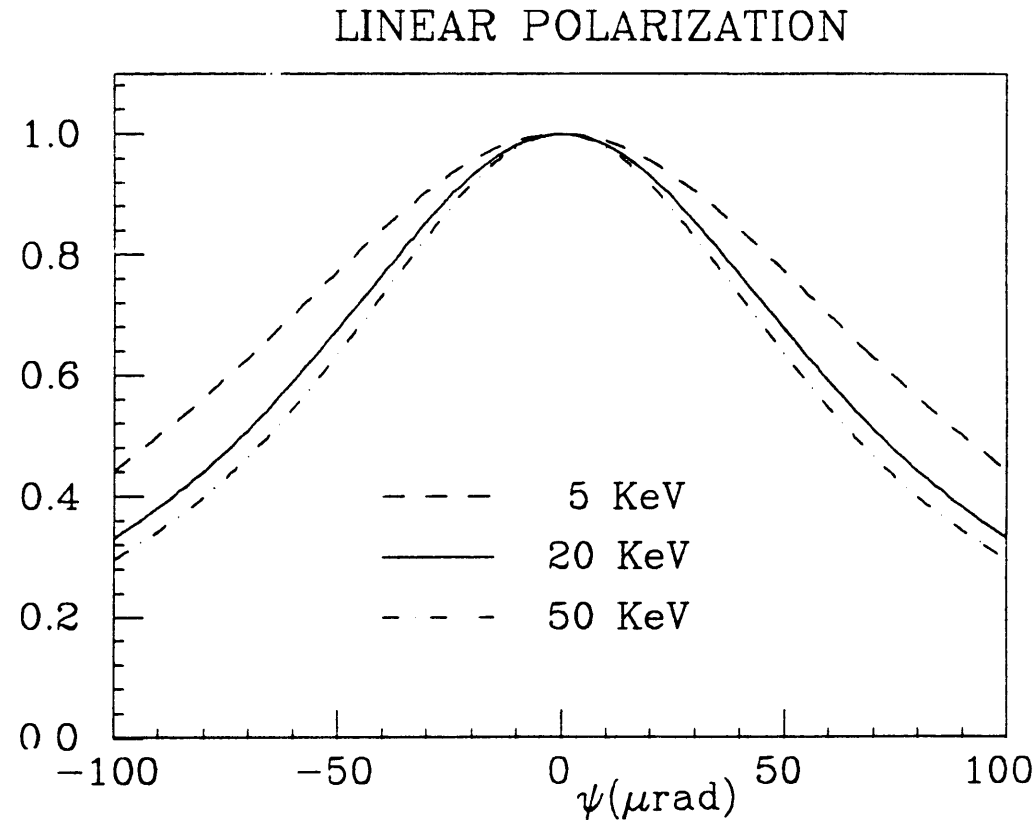

FIG. 8a - Linear polarization from the ESRF bending magnet source.

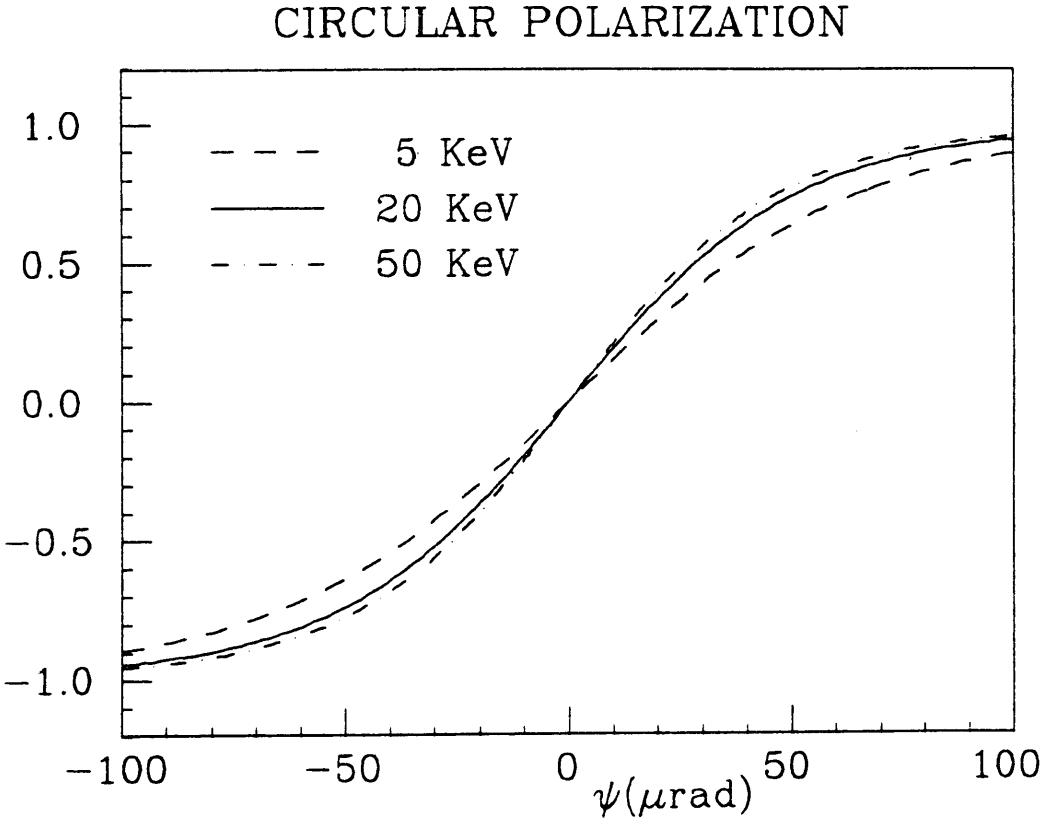

FIG. 8b - Circular polarization from the ESRF bending magnet source.

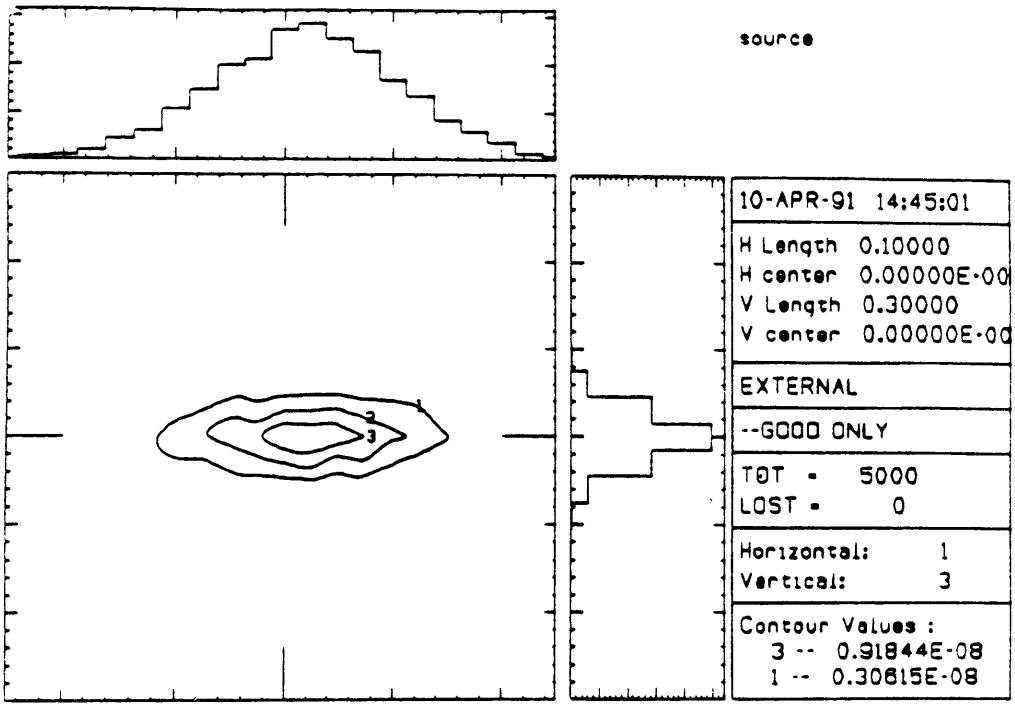

FIG. 9 - Simulation of the source in real space. Horizontal and vertical units are centimeters.

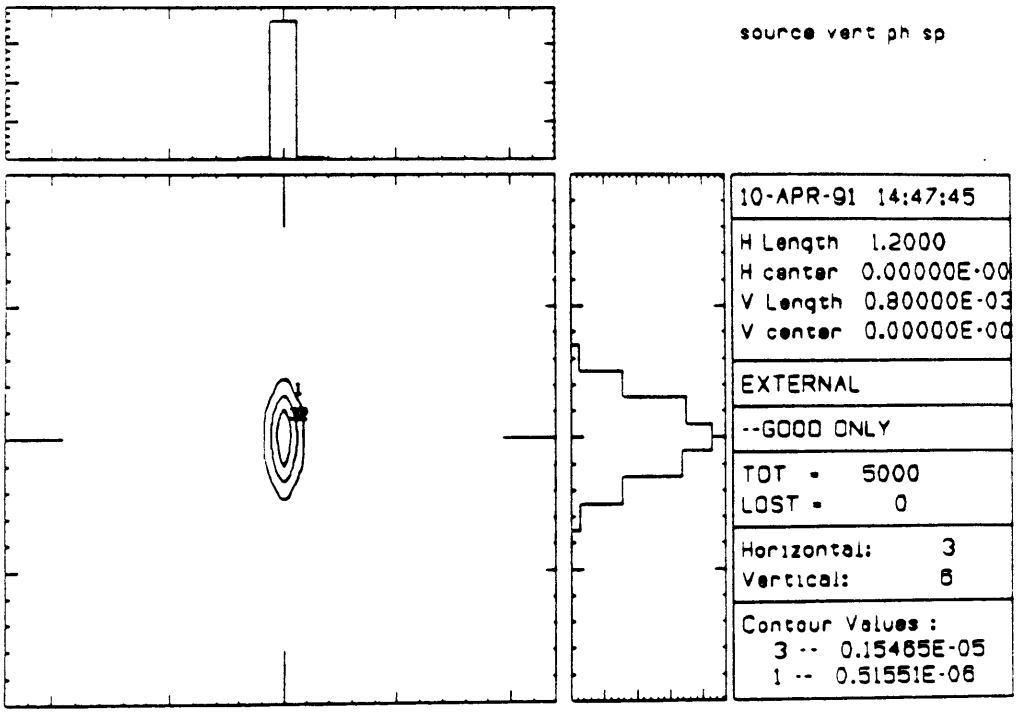

FIG. 10 - Simulation of the source in vertical phase space. Horizontal and vertical units are radians and centimeters, respectively.

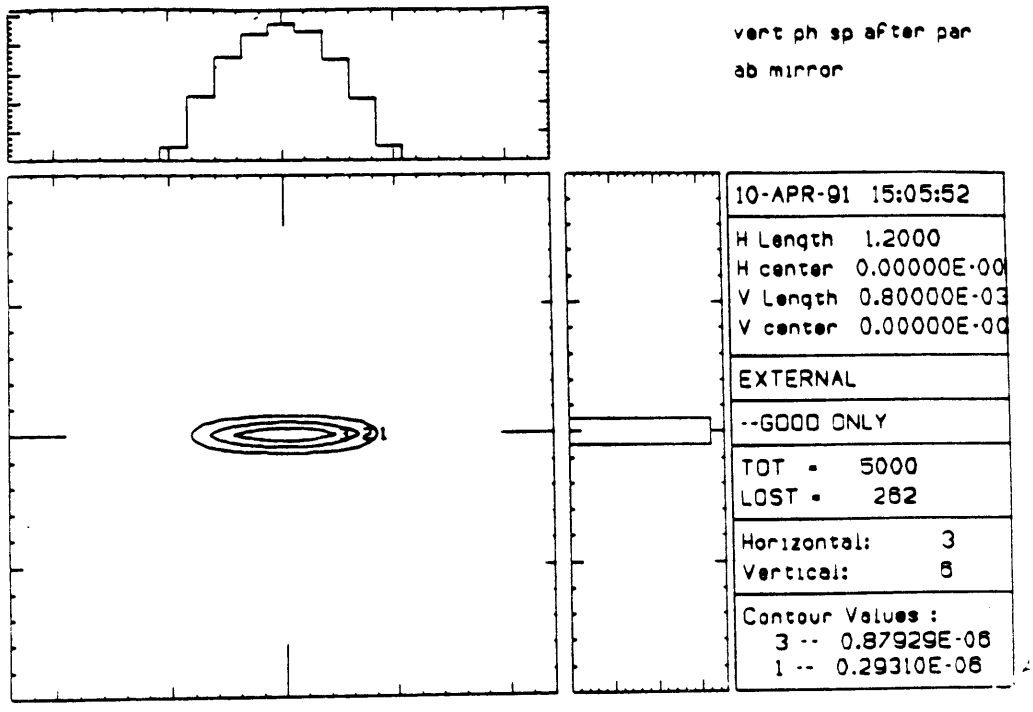

FIG. 11a - Vertical phase space of the beam at 30 m from the source after an ideal parabolic mirror. Horizontal and vertical units are radians and centimeters, respectively.

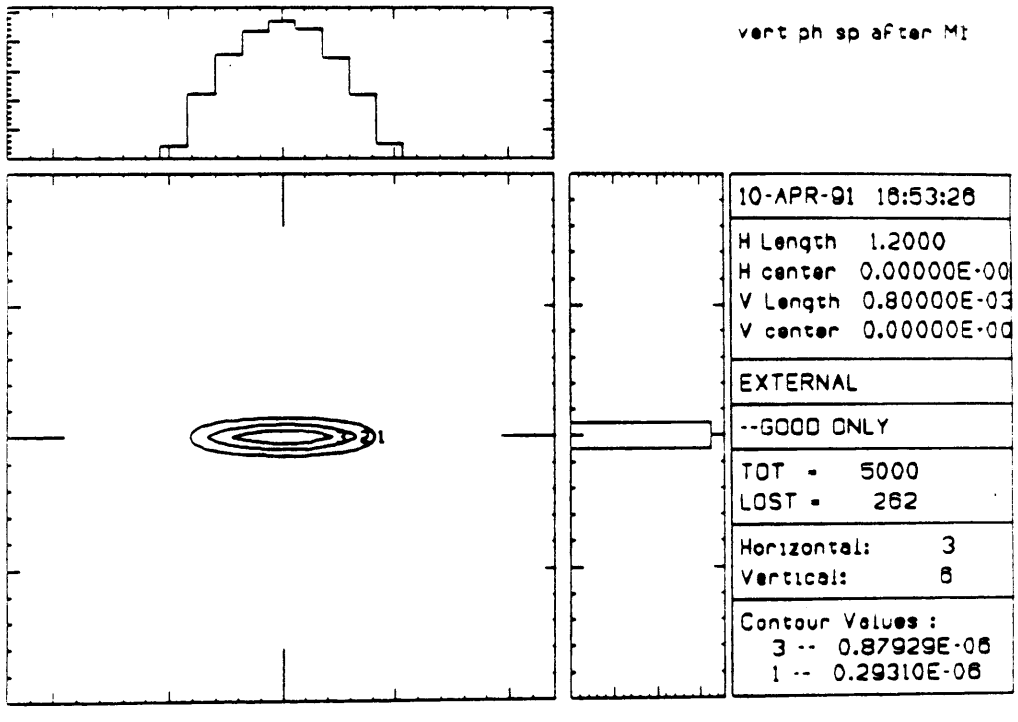

FIG. 11b - Vertical phace space of the beam at 30 m from the source after a cylindrical mirror. Horizontal and vertical units are radians and centimeters, respectively.

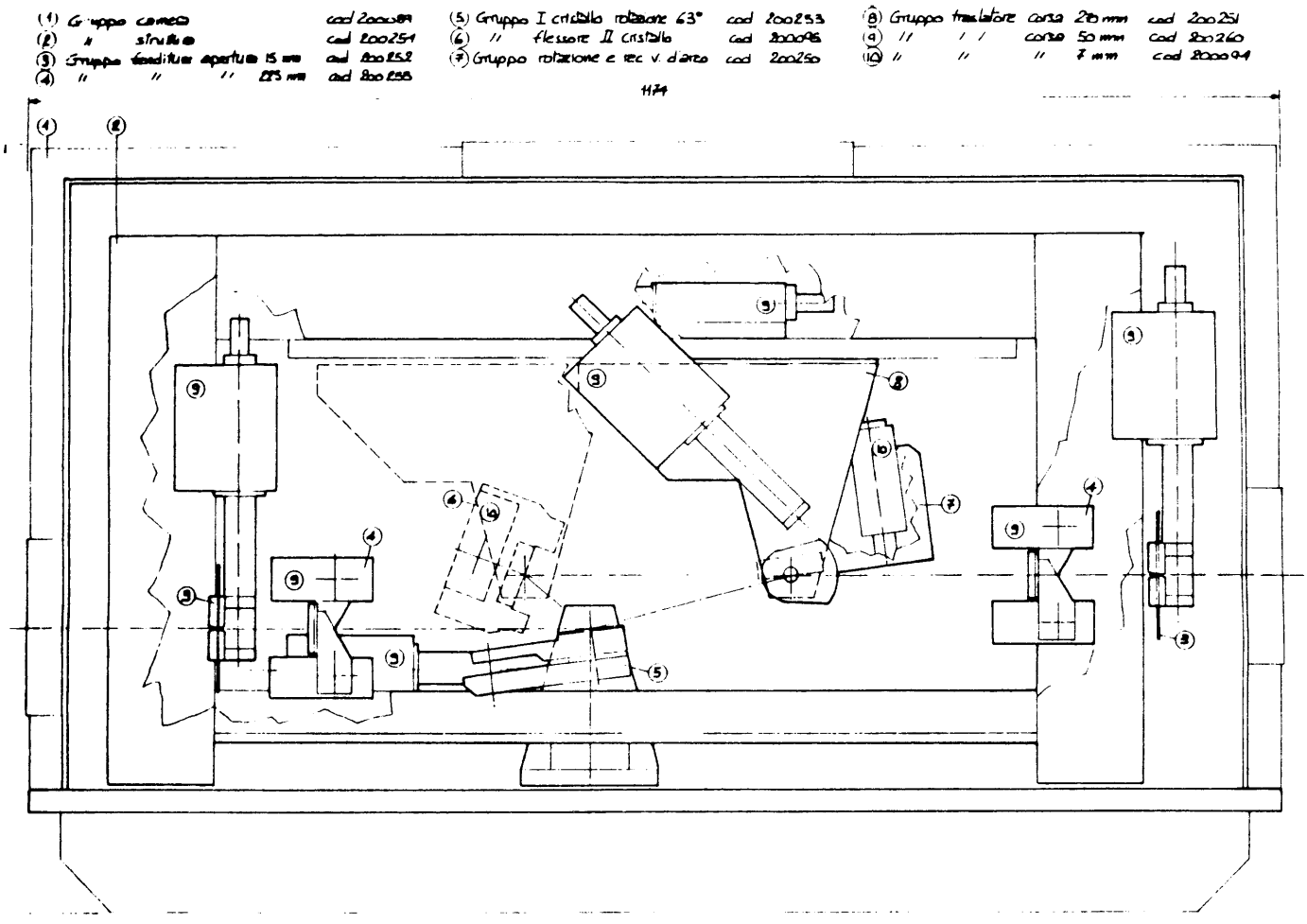

FIG. 12 - Schematic drawing of the monochromator.

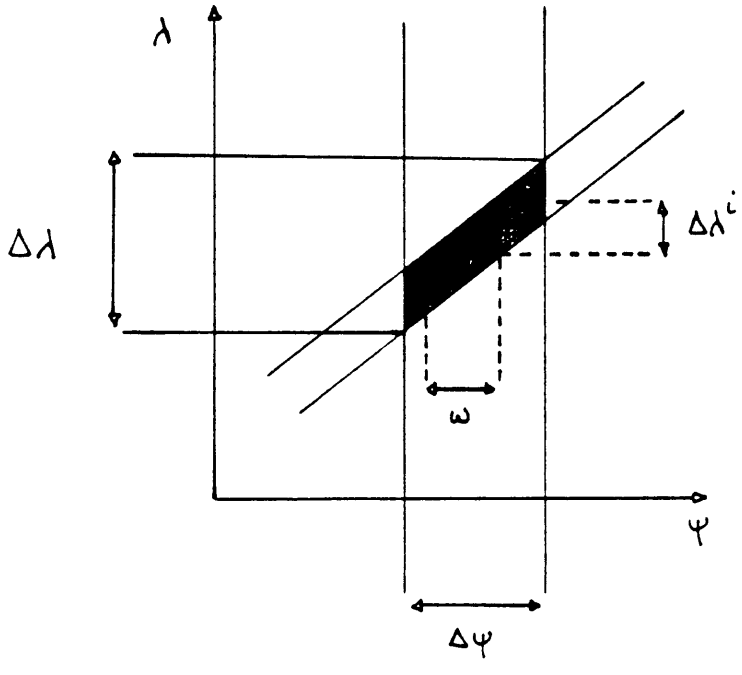

FIG. 13 - Du Mond diagram to visualize the transmission of synchrotron radiation (vertical strip) by a perfect crystal; ω is the Darwin width.

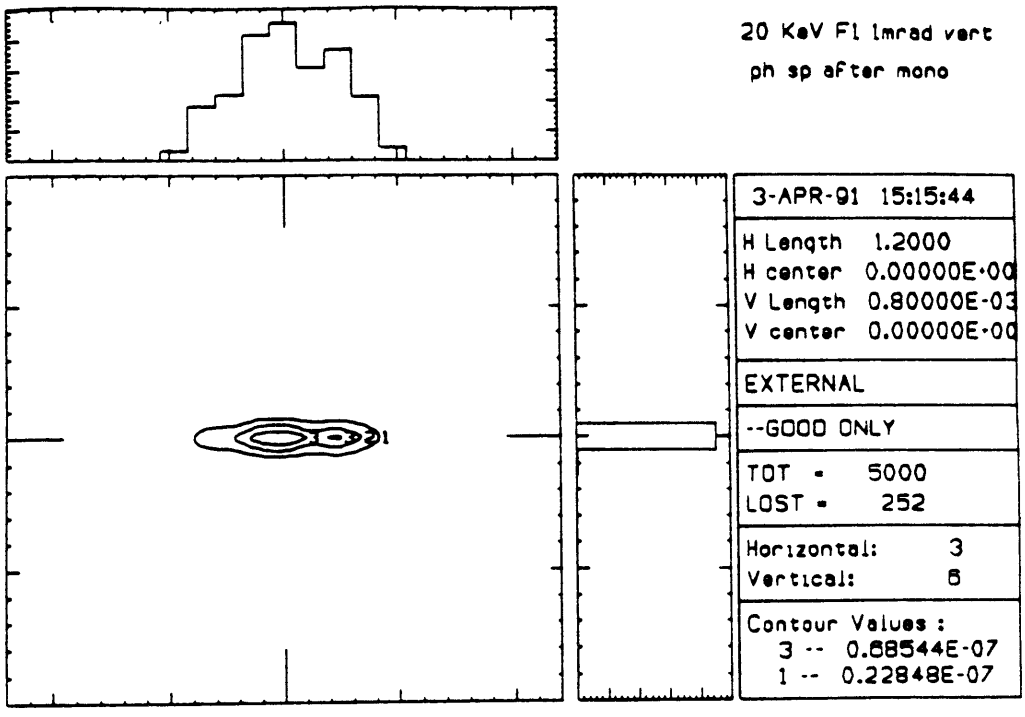

FIG. 14a - Vertical phase space of the beam after the monochromator, at 20 keV for a 1 mrad horizontal acceptance. Horizontal and vertical units are radians and centimeters, respectively.

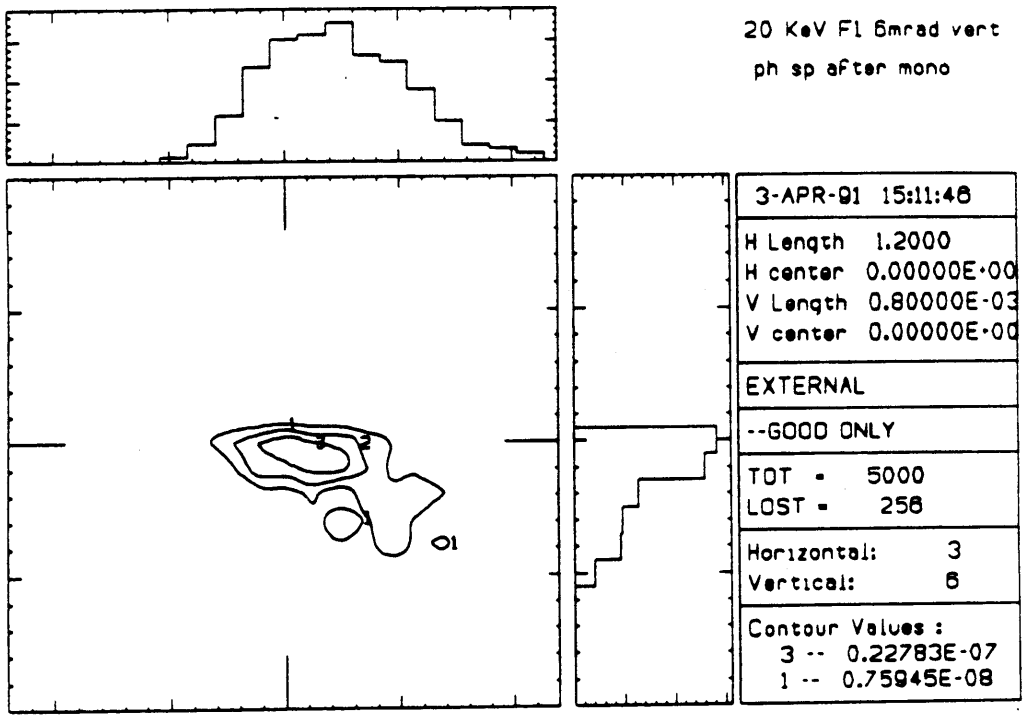

FIG. 14b - Vertical phase space of the beam after the monochromator, at 20 keV for a 6 mrad horizontal acceptance, to illustrate the effect of sagittal focussing aberrations. Horizontal and vertical units are radians and centimeters, respectively.

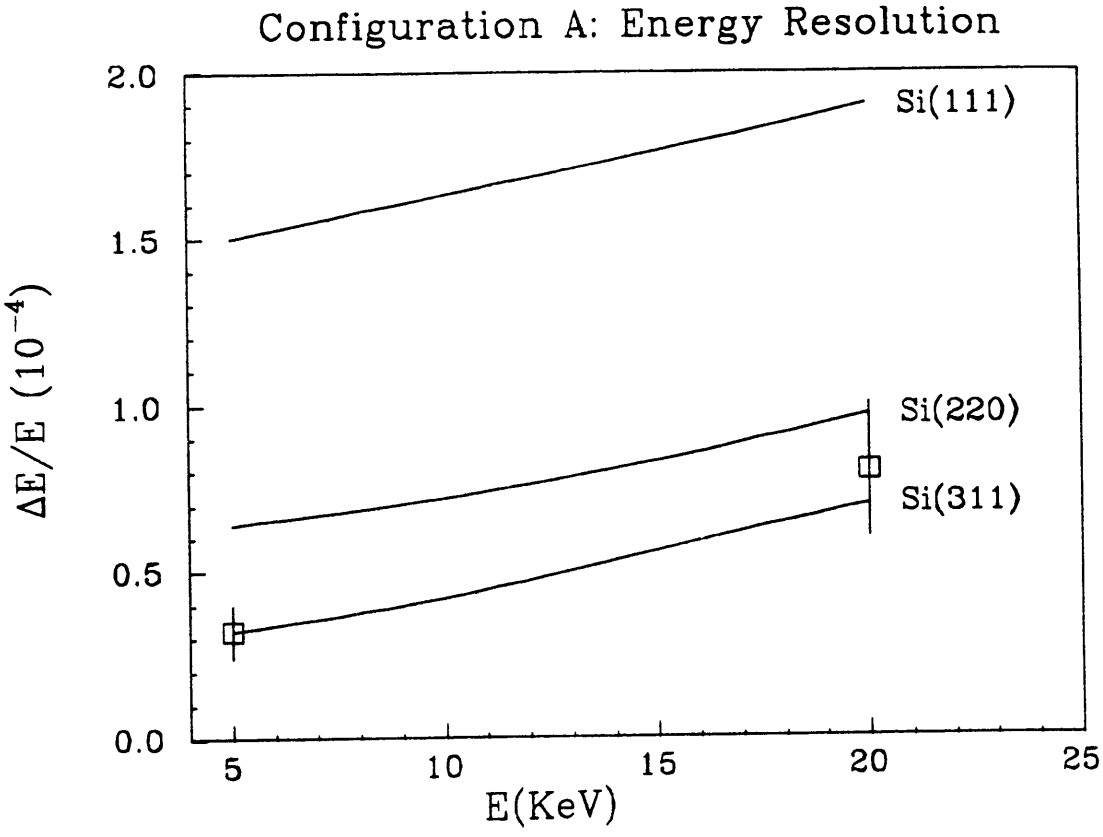

FIG. 15 - Energy resolution in configuration A. The full lines are calculations while the two squares are the results of simulations.

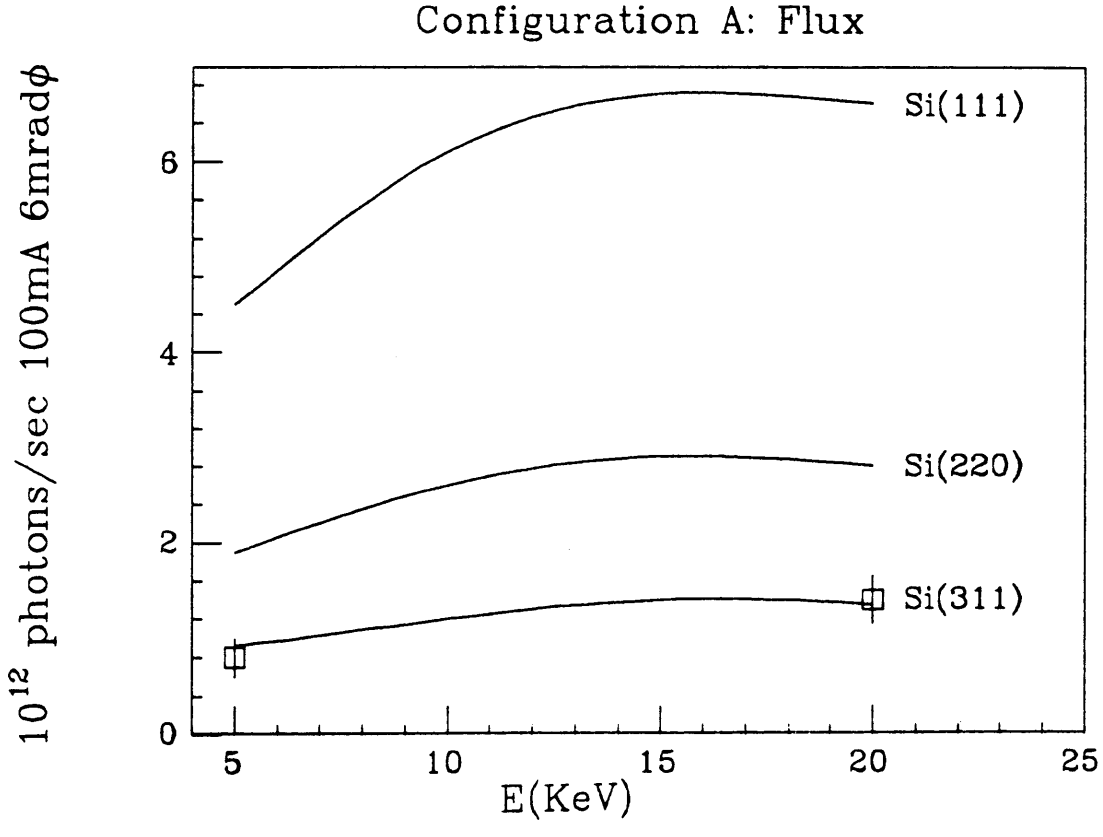

FIG. 16 - Flux in configuration A, at E1 and for 6 mrads.The full lines are calculations while the two squares are the results of simulations.

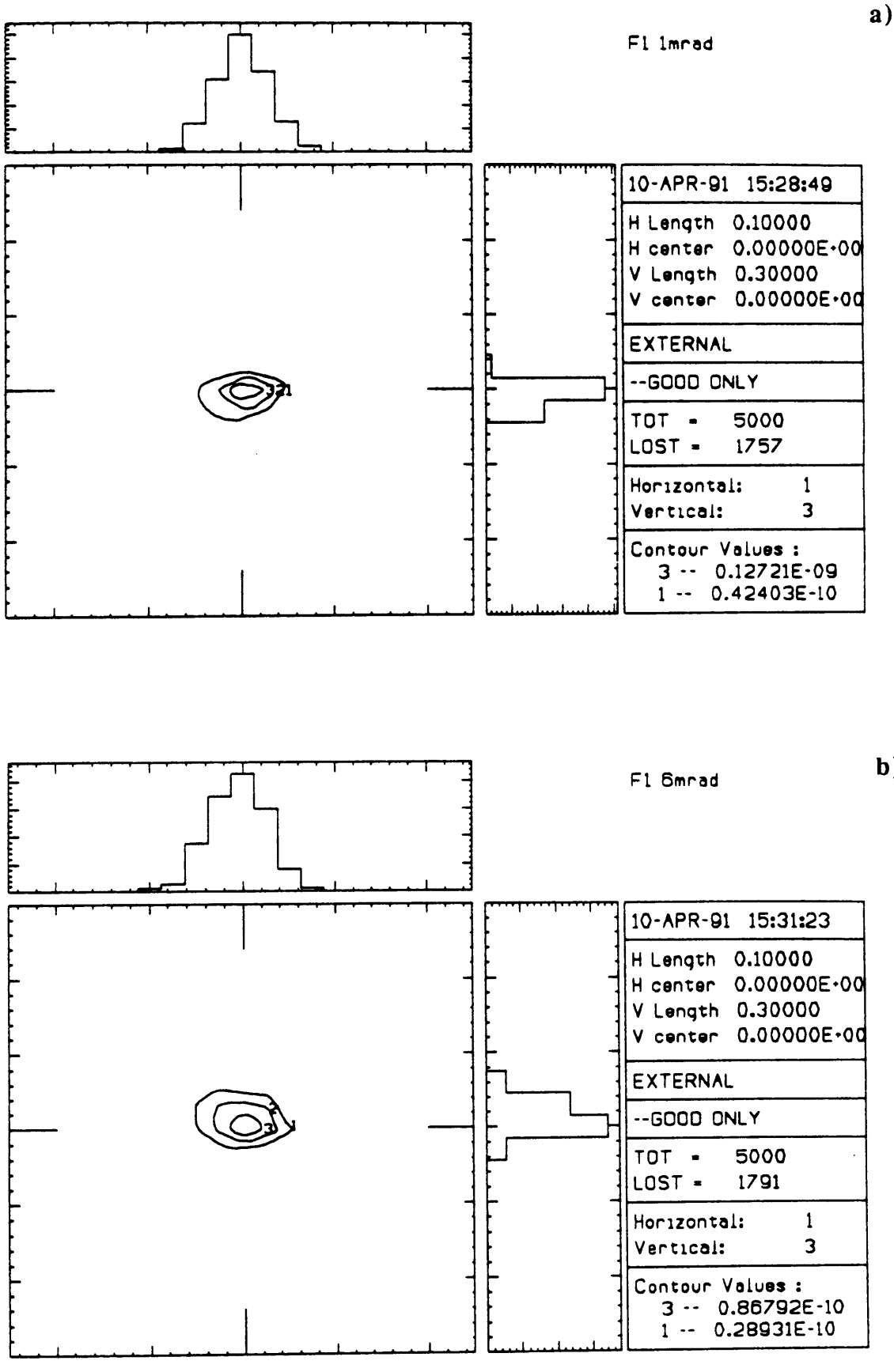

FIG 17 - Images of focal spot for configuration A at 5 keV (units are cm) in E_1 with a) 1 mrad b) 6 mrad.

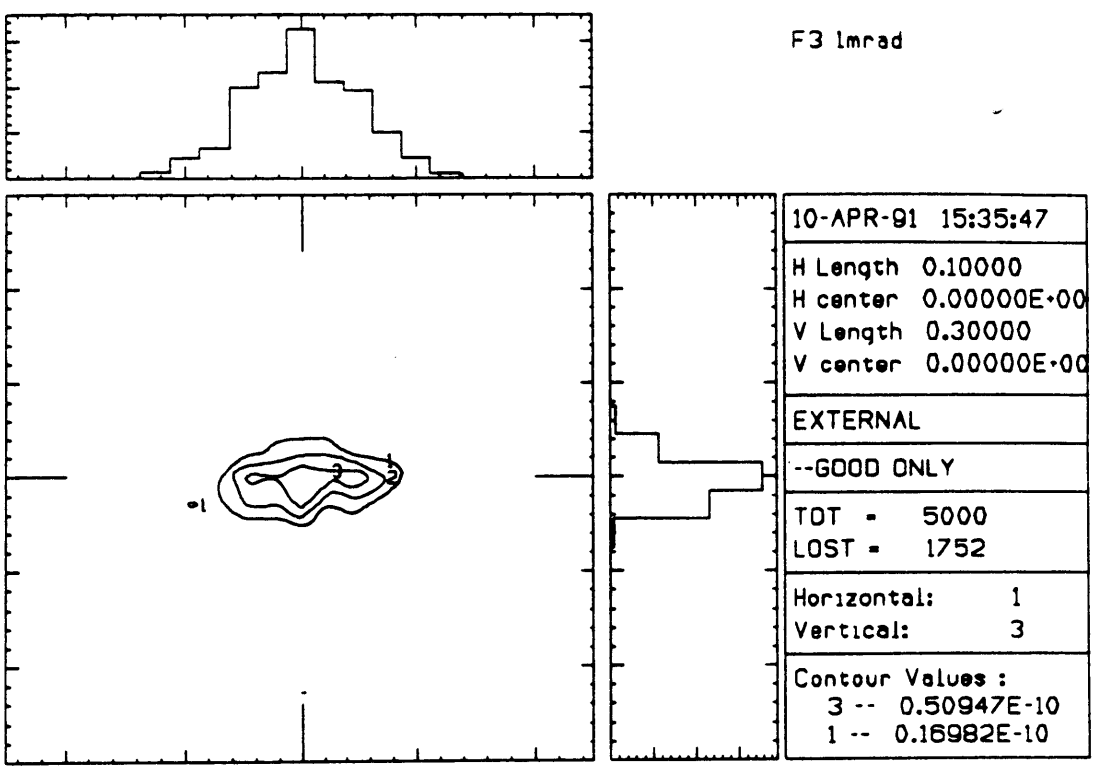

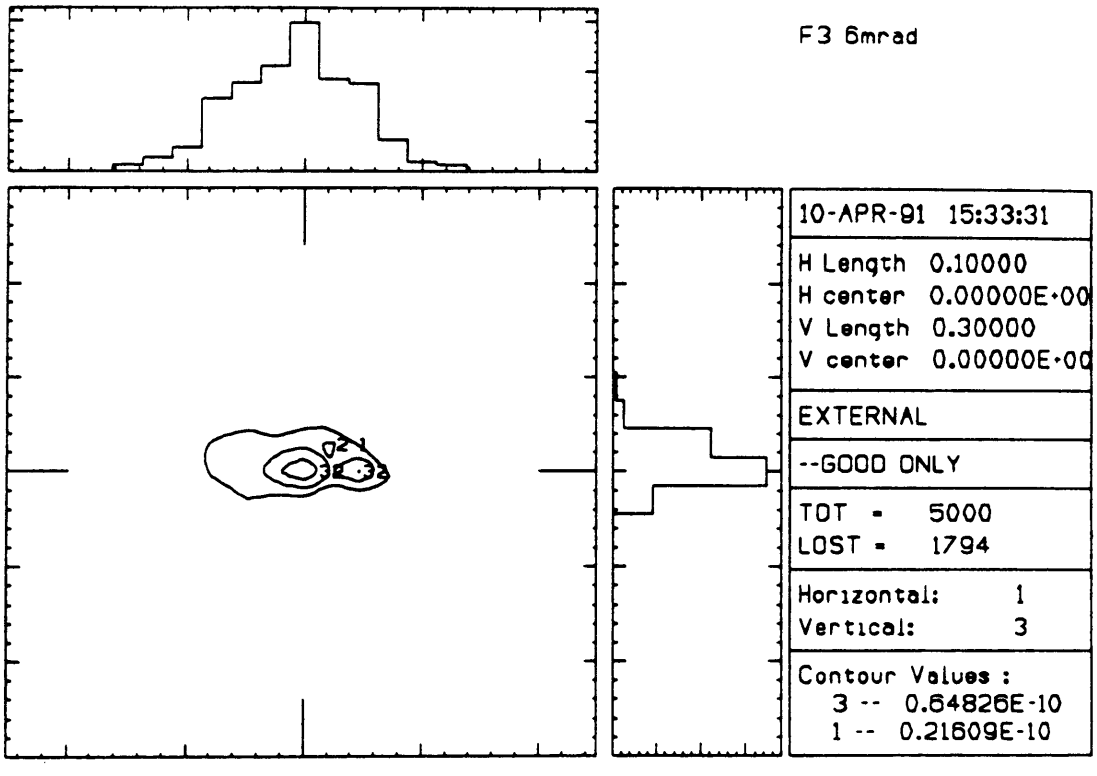

FIG. 17 - Images of focal spot for configuration A at 5 keV (units are cm) in E_3 with c) 1 mrad d) 6 mrad.

a)

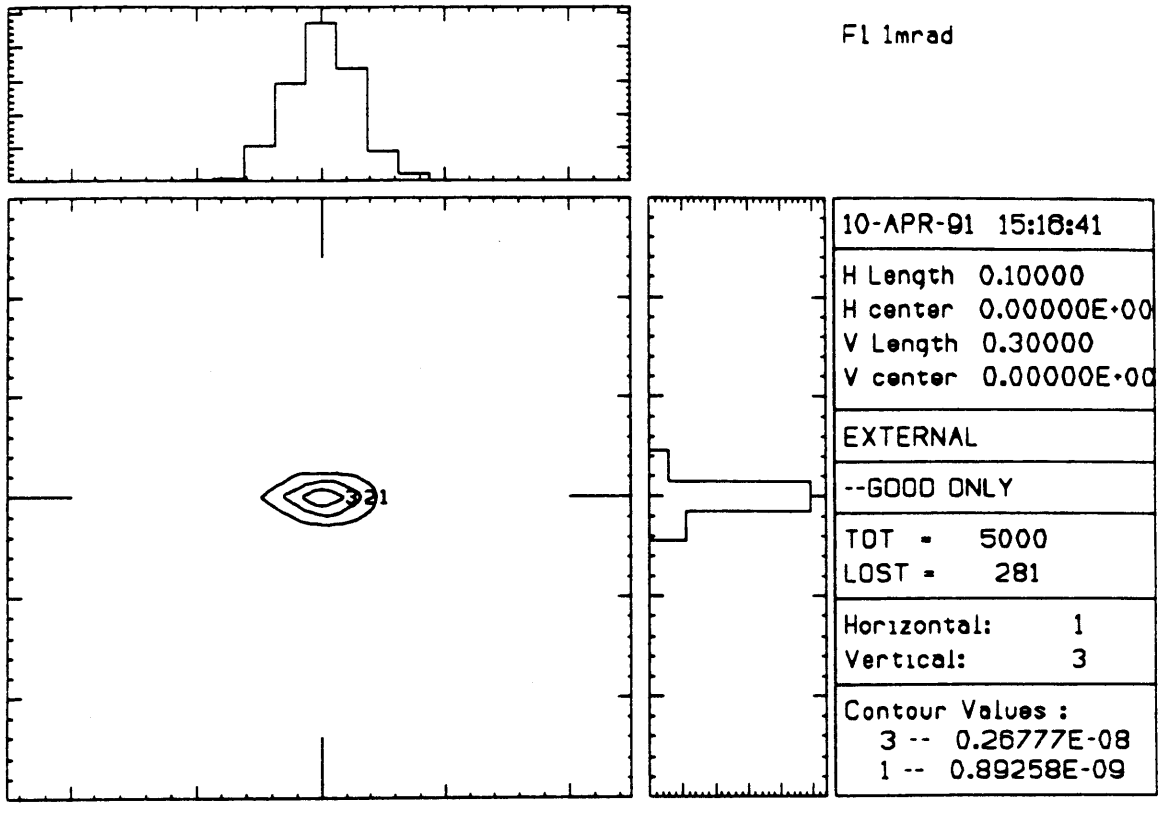

b)

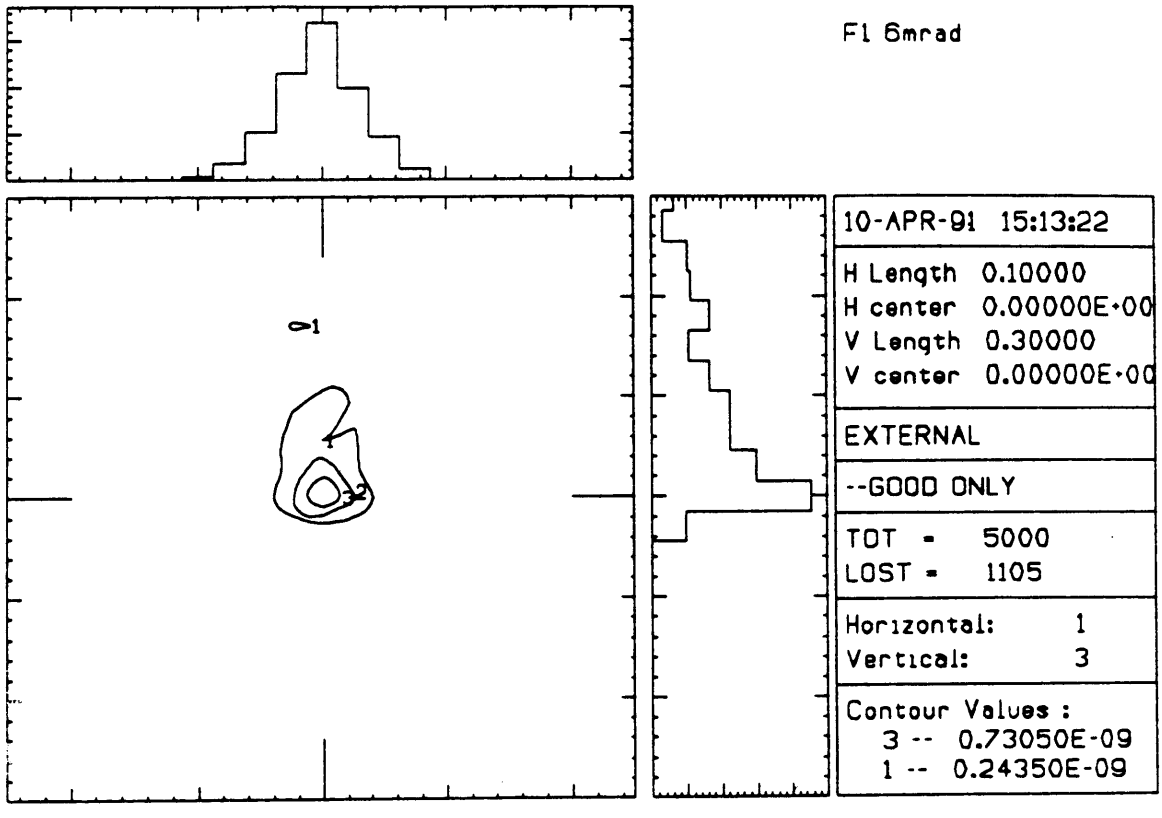

FIG. 18 - Images of focal spot for configuration A at 20 keV (units are cm) in E_1 with a) 1 mrad b) 6 mrad.

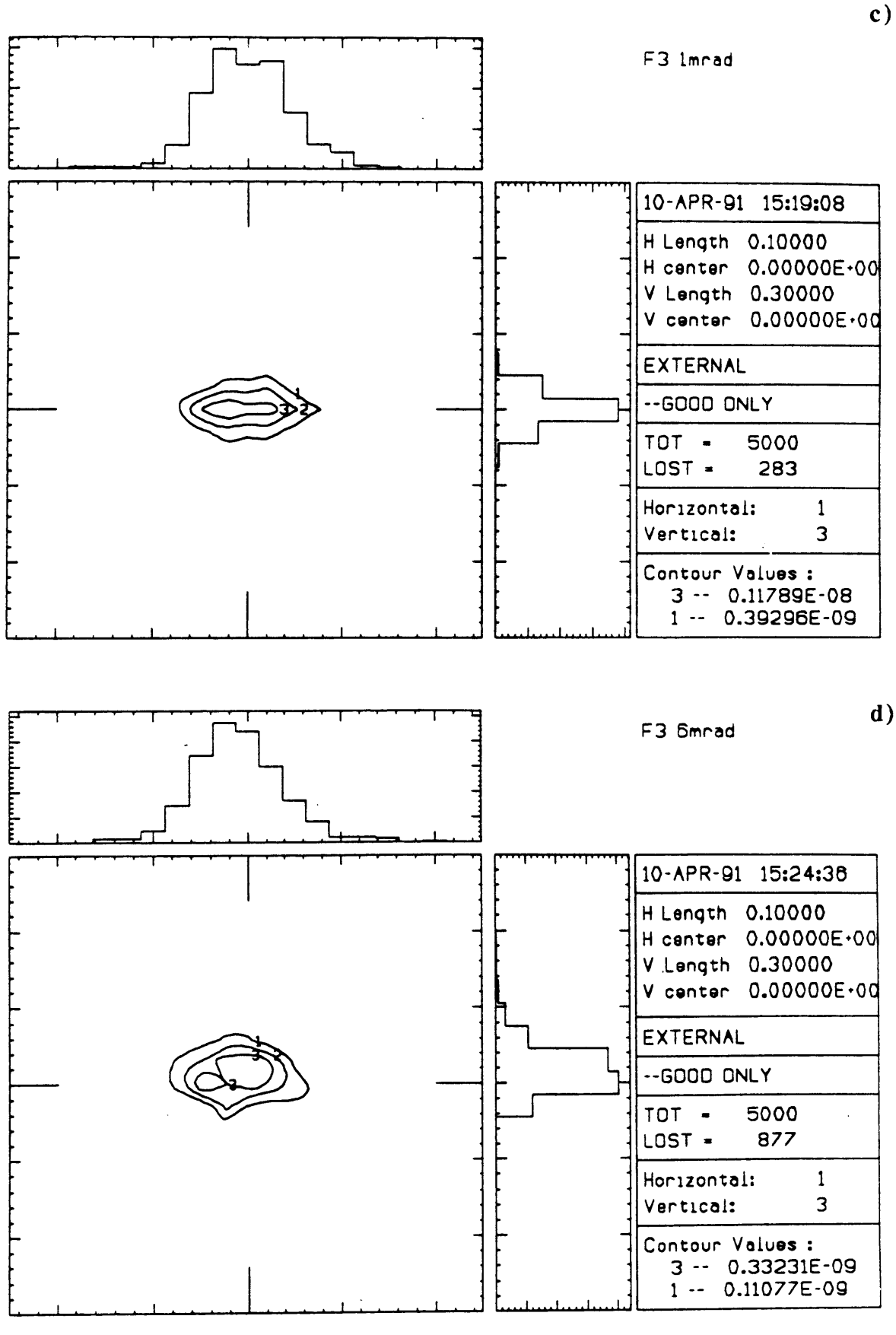

FIG. 18 - Images of focal spot for configuration A at 20 keV (units are cm) in E_3 with c) 1 mrad d) 6 mrad.

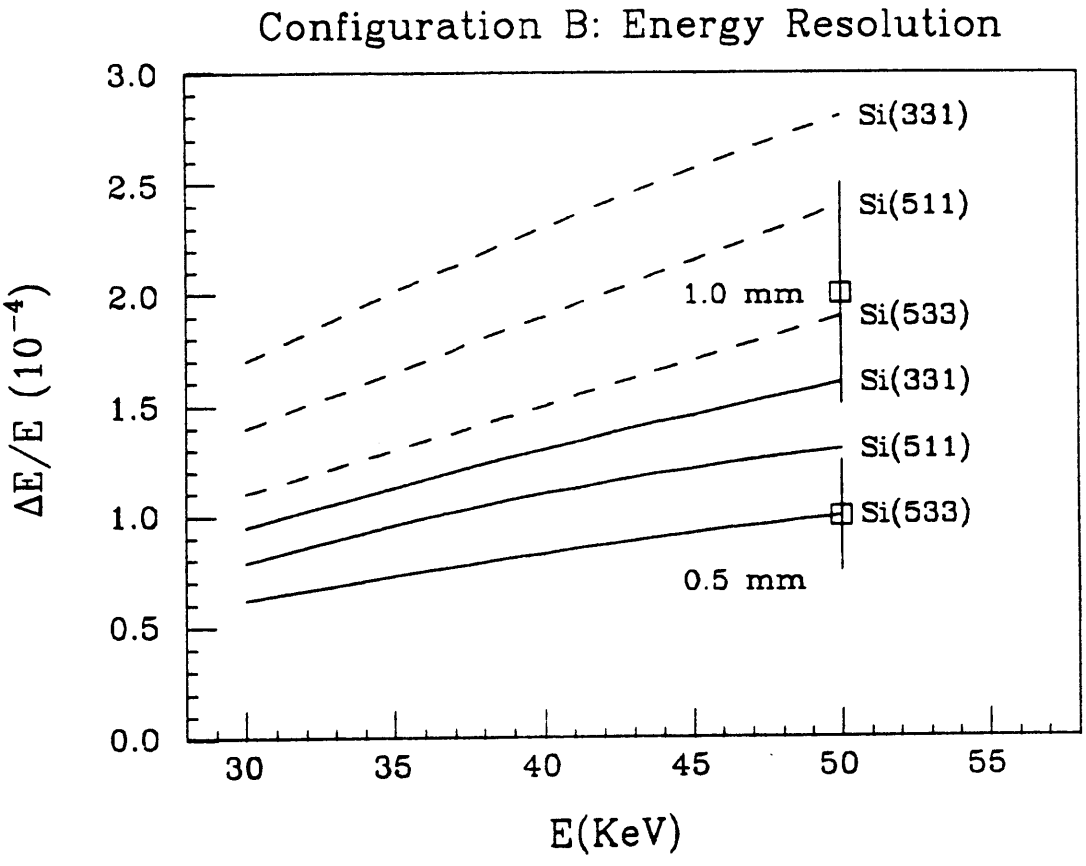

FIG. 19 - Energy resolution in configuration B. The lines (full: 0.5 mm slit; dashed: 1 mm slit) are calculations while the two squares are the results of simulations.

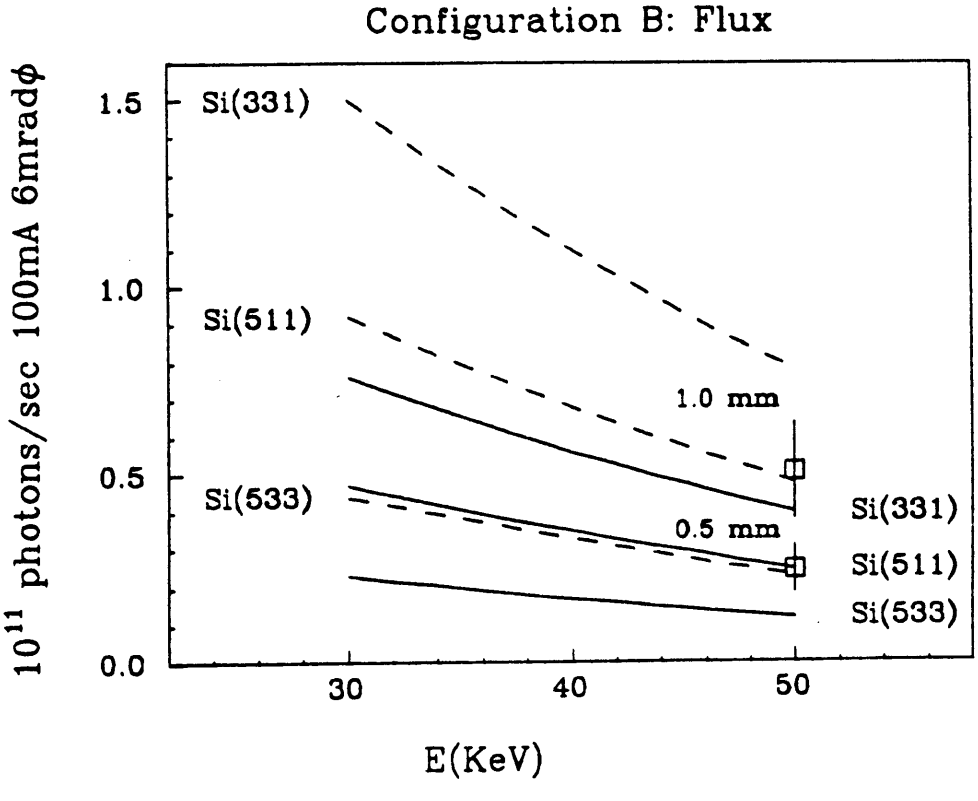

FIG. 20 - Flux in configuration B. The lines (full: 0.5 mm slit; dashed: 1 mm slit) are calculations while the two squares are the results of simulations.

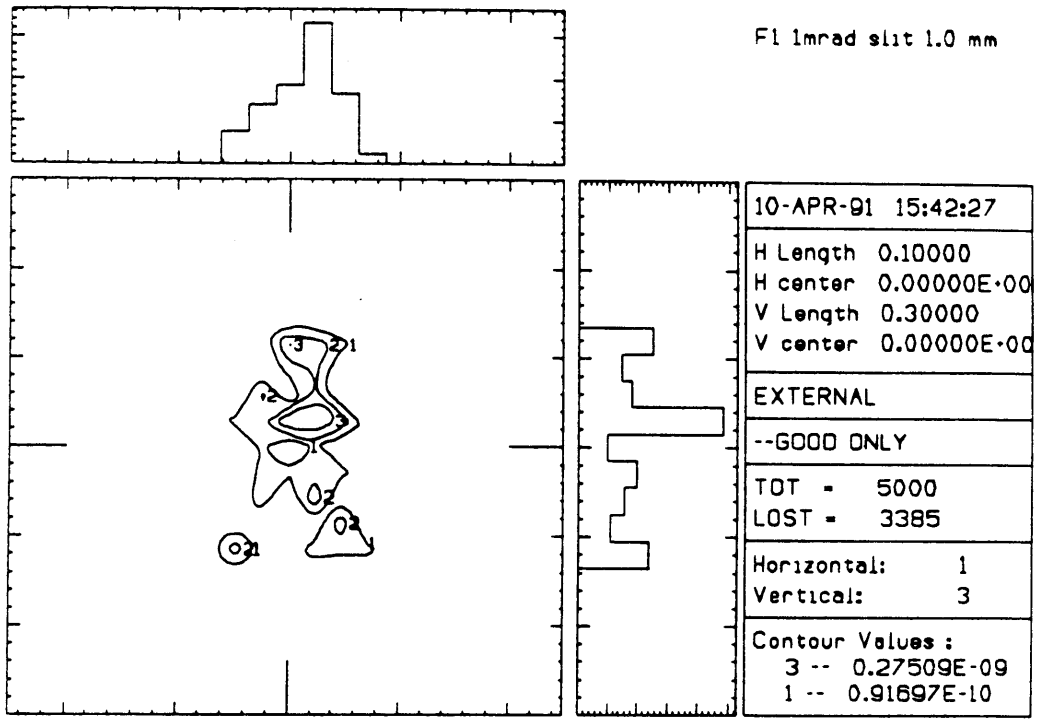

FIG. 21 - Image of focal spot for configuration B at 50 keV in E1 with a 1.0 mm slit (units are cm.).

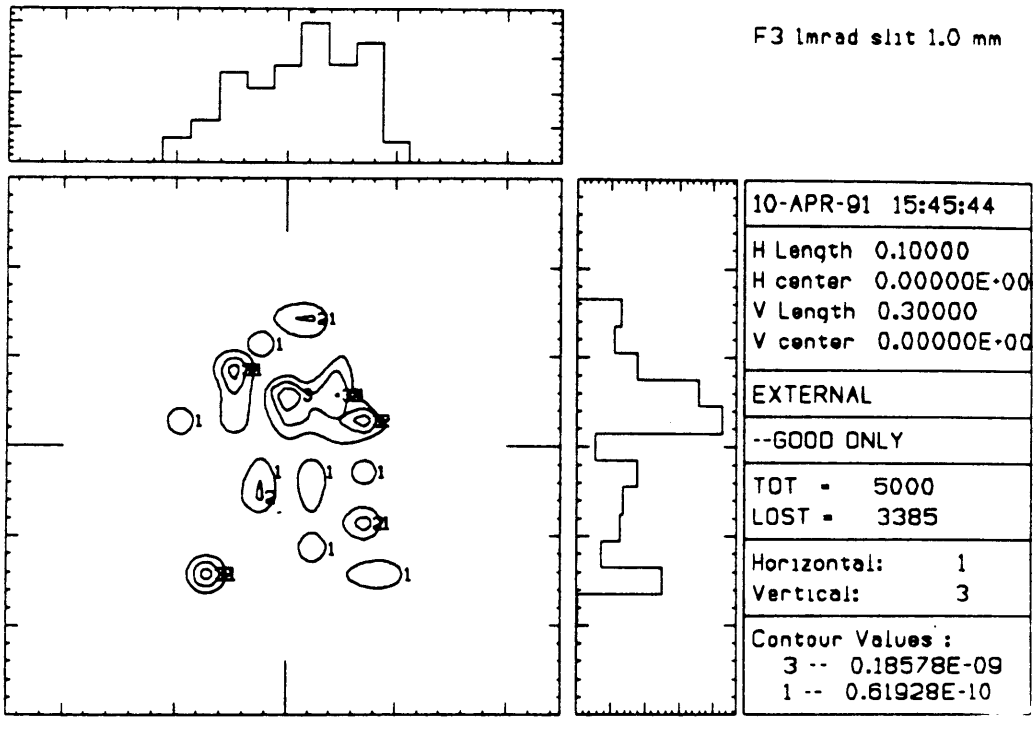

FIG. 22 - Image of focal spot for configuration B at 50 keV in E3 with a 1.0 mm slit (units are cm.).